Monthly Notices
of the
ROYAL ASTRONOMICAL SOCIETY

MNRAS **505,** 4197–4214 (2021)
Advance Access publication 2021 May 14

https://doi.org/10.1093/mnras/stab1330

Magnetohydrodynamic effect on first star formation: pre-stellar core collapse and protostar formation

Kenji Eric Sadanari,[1]★ Kazuyuki Omukai,[1] Kazuyuki Sugimura,[1,2] Tomoaki Matsumoto[3] and Kengo Tomida[1]

[1]*Astronomical Institute, Tohoku University, Aoba, Sendai, Miyagi 980-8578, Japan*
[2]*Department of Astronomy, University of Maryland, College Park, MD 20740, USA*
[3]*Faculty of Sustainability Studies, Hosei University, Fujimi, Chiyoda, Tokyo 102-8160, Japan*

Accepted 2021 May 6. Received 2021 May 5; in original form 2021 March 12

ABSTRACT

Recent theoretical studies have suggested that a magnetic field may play a crucial role in the first star formation in the universe. However, the influence of the magnetic field on the first star formation has yet to be understood well. In this study, we perform three-dimensional magnetohydrodynamic simulations taking into account all the relevant cooling processes and non-equilibrium chemical reactions up to the protostar density, in order to study the collapse of magnetized primordial gas cores with self-consistent thermal evolution. Our results show that the thermal evolution of the central core is hardly affected by a magnetic field because magnetic forces do not prevent the contraction along the field lines. We also find that the magnetic braking extracts the angular momentum from the core and suppresses fragmentation depending on the initial strength of the magnetic field. The angular momentum transport by the magnetic outflows is less effective than that by the magnetic braking because the outflows are launched only in a late phase of the collapse. Our results indicate that the magnetic effects become important for the field strength $B > 10^{-8}(n_{\rm H}/1\ {\rm cm}^{-3})^{2/3}$ G, where $n_{\rm H}$ is the number density, during the collapse phase. Finally, we compare our results with simulations using a barotropic approximation and confirm that this approximation is reasonable at least for the collapse phase. Nevertheless, self-consistent treatment of the thermal and chemical processes is essential for extending simulations to the accretion phase, in which radiative feedback by protostars plays a crucial role.

Key words: stars: formation – stars: magnetic field – stars: Population III.

1 INTRODUCTION

The first stars, also known as the Pop III stars, are thought to have formed around the redshift $z \sim 20$–30 in minihaloes of $M \sim 10^6\,M_\odot$ (Couchman & Rees 1986; Yoshida et al. 2003; Greif 2015). They play crucial roles in the subsequent structure formation in the universe. For example: ionizing photons emitted from these stars start reionizing the intergalactic medium; their supernovae spread heavy elements into the interstellar medium, which drive the chemical evolution of the universe (e.g. Ciardi & Ferrara 2005). The first stars are formed from the primordial gas, which lacks metals and dust grains. Only available coolant in the low temperature ($< 10^4$ K) is molecular hydrogen H_2, resulting in rather high temperature of several hundred K during the pre-stellar collapse and thus high accretion rate $\sim 10^{-3}\,M_\odot$ yr^{-1} on to the formed protostar (Stahler, Palla & Salpeter 1986; Omukai & Nishi 1998). The high accretion rate causes formation of massive stars with 10–1000 $M_\odot$ (Abel, Bryan & Norman 2002; Bromm, Coppi & Larson 2002; Omukai & Palla 2003; McKee & Tan 2008; Yoshida, Omukai & Hernquist 2008; Hosokawa et al. 2016; Stacy, Bromm & Lee 2016), and their initial mass function (IMF) is expected to be top heavy (Hirano et al. 2014; Susa, Hasegawa & Tominaga 2014).

Previous works have demonstrated by three-dimensional (3D) simulations that first stars tend to be in binary (or multiple) systems as a result of pre-stellar fragmentation during the collapse or circumstellar disc fragmentation in the accretion phase (e.g. Machida et al. 2008b; Clark et al. 2011; Smith et al. 2011; Stacy et al. 2016; Susa 2019; Chon & Hosokawa 2019; Kimura, Hosokawa & Sugimura 2021). Sugimura et al. (2020) have performed 3D radiation hydrodynamics simulations starting from the onset of the gravitational collapse to the end of accretion, and have found the formation of a similar-mass binary system consisting of stars with 56 and 66 $M_\odot$ at a separation of 2×10^4 au. Such a massive binary is expected to evolve into a black hole (BH) binary system. If close enough, a BH binary merges within the age of the universe and can be sources of observed gravitational wave (GW) events. Recent population synthesis calculations (e.g. Kinugawa et al. 2014, 2016) suggest that $\sim 30\,M_\odot$ BH binaries observed by GWs are originated from the first star.

Those 3D simulations, however, have not included effects of the magnetic field. In nearby star-forming regions, magnetic fields of several μG are known to exist. Such strong fields in the present-day universe are believed to be originated from amplification of weak seed fields by galactic dynamo processes (e.g. Brandenburg & Subramanian 2005; Pakmor et al. 2017). From a theoretical point of view, seed fields of 10^{-20}–10^{-10} G can be generated from astrophysical mechanisms involving the battery effect (Biermann 1950) due to supernovae (Hanayama et al. 2005), galaxy formation

★ E-mail: k.sadanari@astr.tohoku.ac.jp

(Kulsrud et al. 1997), reionization (Gnedin, Ferrara & Zweibel 2000; Attia et al. 2021), and radiation pressure from the radiation sources (Langer, Puget & Aghanim 2003; Doi & Susa 2011). Seed fields could also be generated in the very early universe during the electroweak and QCD phase transitions (e.g. Quashnock, Loeb & Spergel 1989; Baym, Bödeker & McLerran 1996; Banerjee & Jedamzik 2004; Durrer & Neronov 2013; Subramanian 2016), although the generated field strength rely highly on uncertainties in the adopted models. In addition, Ichiki et al. (2006) show that the cosmological fluctuations can generate seed magnetic fields of about 10^{-24} G at 1 Mpc scale during the recombination epoch. It is thus likely that seed magnetic fields already existed before the formation of first stars. Such weak fields, however, have little effects on the first star formation. In order to drive a protostellar jet during collapse phase, the host cloud with the density of about 1 cm^{-3} needs to have a field stronger than 10^{-11} G (Machida, Matsumoto & Inutsuka 2008c). Therefore magnetic fields play a significant role in the first star formation only if the seed field can be sufficiently amplified. Schober et al. (2012) have investigated the amplification of magnetic fields by small-scale dynamo during the collapse of a turbulent first-star-forming cloud by one-zone calculation and found that the field increases exponentially immediately after the onset of the collapse and reaches the level as strong as $\sim 10^{-6}$ G. The small-scale dynamo is also shown to be effective in amplifying the magnetic field by 3D hydrodynamical simulations (e.g. Sur et al. 2010; Federrath et al. 2011; Turk et al. 2012; Sharda et al. 2021). With amplification of small initial seeds, magnetic fields may have substantial effects on the first star formation.

3D magnetohydrodynamic (MHD) simulations for the first star formation have already been performed (e.g. Machida et al. 2008c; Sharda, Federrath & Krumholz 2020). Machida et al. (2008c) have calculated pre-stellar collapse of primordial-gas clouds until the protostar formation at 10^{21} cm^{-3} with different sets of the initial rotation and magnetic energy by 3D MHD simulations, and investigated the condition for fragmentation and outflow launching. They found that if the initial magnetic field has higher energy than that of the cloud rotation, the angular momentum of the cloud is transported by the magnetic braking and suppresses the formation of a rotation-supported disc and its fragmentation. They also showed that MHD winds are driven in models in which the fragmentation does not occur. In such cases, MHD winds may play an important role in setting the star formation efficiency in cloud cores, as in the present-day star formation. Recently, Sharda et al. (2020) showed that even weaker magnetic fields (10^{-15} G) can affect the IMF of first stars by extending simulations to the accretion phase.

However, Machida et al. (2008c) used the barotropic approximation for the gas equation of state, where the temperature is given as a function of density, based on the result of the one-zone calculation (Omukai et al. 2005), without solving the thermal evolution of gas consistently. Effects such as shock heating and back-reaction of strong magnetic fields on the temperature evolution (Nakauchi, Omukai & Susa 2019) cannot be properly incorporated in barotropic simulations. It is not clear to what extent these effects influence the dynamics, such as the cloud fragmentation by changing the temperature evolution.

In this work, we reveal magnetic effects on the collapse of primordial-gas cloud cores by solving the thermal evolution and gas dynamics consistently. To this end, for the first time, we perform 3D MHD simulations of collapse phase taking into account all the relevant cooling processes and non-equilibrium chemical reaction up to the protostar density. We also perform barotropic simulations for comparison and discuss the validity of this approximation.

This paper is organized as follows. In Section 2, we describe the method and setup of our simulations. We present the results in Section 3. In Section 3.1, we first focus on the evolution of non-rotating clouds to see magnetic field effects on the central temperature evolution, and in Section 3.2, we present the results for magnetized rotating clouds to see effects of the magnetic braking and outflows. In Section 3.3, we discuss the fragmentation and outflow-launching conditions for the rotational and magnetic energy of the initial cloud. Finally, in Section 3.4, we compare our results with those obtained with the barotropic approximation and discuss its validity. In Section 4, we summarize our findings and discuss magnetic field effects on the first star formation.

2 NUMERICAL METHOD

We follow collapsing cloud evolution by using a magnetohydrodynamics code SFUMATO (Matsumoto 2007; Matsumoto, Dobashi & Shimoikura 2015) with adaptive mesh refinement (AMR) and self-gravity. The MHD part is solved by the HLLD approximation Riemann solver (Miyoshi & Kusano 2005) with a mixed divergence cleaning method (Dedner et al. 2002), and the self-gravity part is solved by a multigrid method. These two schemes have a second-order accuracy in space and time. We modify SFUMATO by introducing a module solving the chemical and thermal evolution of primordial gas, which is used in a radiative hydrodynamics version of the code, SFUMATO-RT (Sugimura et al. 2020). In addition, since the thermal processes in the SFUMATO-RT are only relevant in the density range $n_{\rm H} < 10^{13}$ cm^{-3}, we add the chemical and cooling processes that are important in a higher density region to solve until the protostar formation.

The governing equations are as follows: the mass conservation,

$$\frac{\partial \rho}{\partial t} + \nabla \cdot (\rho \boldsymbol{v}) = 0, \tag{1}$$

the equation of motion,

$$\rho \frac{\partial \boldsymbol{v}}{\partial t} + \rho (\boldsymbol{v} \cdot \nabla) \boldsymbol{v} = -\nabla p - \frac{1}{4\pi} \boldsymbol{B} \times (\nabla \times \boldsymbol{B}) - \rho \nabla \phi, \tag{2}$$

the gas energy equation,

$$\frac{\partial e}{\partial t} + \nabla \cdot \left[\left(e + p + \frac{|\boldsymbol{B}|^2}{8\pi} \right) \boldsymbol{v} - \frac{1}{4\pi} \boldsymbol{B} (\boldsymbol{v} \cdot \boldsymbol{B}) \right] = -\rho \boldsymbol{v} \cdot \nabla \phi - \Lambda, \tag{3}$$

the induction equation of ideal MHD,

$$\frac{\partial \boldsymbol{B}}{\partial t} = \nabla \times (\boldsymbol{v} \times \boldsymbol{B}), \tag{4}$$

the solenoidal constraint,

$$\nabla \cdot \boldsymbol{B} = 0, \tag{5}$$

and the Poisson equation of the gravity,

$$\nabla^2 \phi = 4\pi G \rho, \tag{6}$$

where ρ, p, $\boldsymbol{v}$, $\boldsymbol{B}$, ϕ, e, and Λ are the gas density, gas pressure, gas velocity, magnetic field, gravitational potential, total gas energy per unit volume, and net cooling rate per unit volume, respectively. The energy density e is given by

$$e = \frac{1}{2} \rho |\boldsymbol{v}|^2 + \frac{p}{\gamma - 1} + \frac{1}{8\pi} |\boldsymbol{B}|^2, \tag{7}$$

where γ is the adiabatic index, which depends on the chemical composition and gas temperature (e.g. Omukai & Nishi 1998).

We initially take a cube with $L_{\rm box} = 4 \times 10^6$ au on one side as the computational domain and set base grids with $N_{\rm base} = 64$ cells in each direction. When the width of the cell $h(l)$ at the grid level l exceeds 1/16 of the local Jeans length, the cell is refined with the grid level raised to $l + 1$. The cell width is halved at each refinement of the grid: $h(l + 1) = h(l)/2$. We set the maximum grid level $l_{\rm max} = 25$, and thus the minimum width of the cell in this simulation is $\Delta x_{\rm min} = L_{\rm box}/N_{\rm base} \times 2^{-l_{\rm max}} \simeq 2 \times 10^{-3}$ au. In our simulation, we calculate the cloud collapse until the protostar formation at $n_{\rm H} \simeq 10^{20}$ cm^{-3} without using sink particles.

2.1 Thermal and chemical processes

The net cooling rate Λ in equation (3) is given as

$$\Lambda = \Lambda_{\rm line} + \Lambda_{\rm cont} + \Lambda_{\rm chem}, \tag{8}$$

where $\Lambda_{\rm line}$, $\Lambda_{\rm cont}$, and $\Lambda_{\rm chem}$ are the line cooling, continuum cooling, and chemical cooling/heating, respectively. The line cooling consists of the H_2 and HD cooling: $\Lambda_{\rm line} = \Lambda_{H_2} + \Lambda_{\rm HD}$. The H_2 and HD line cooling rate is calculated as

$$\Lambda_{\rm M} = \bar{\beta}_{\rm esc,M} {\rm e}^{-\tau} \Lambda_{\rm M,thin}, \tag{9}$$

where M represents the molecular species H_2 or HD, and the optically thin cooling rate $\Lambda_{\rm M,\,thin}$ is taken from the fitting function of Glover (2015) and Lipovka, Núñez-López & Avila-Reese (2005) for H_2 and HD, respectively. The photon trapping effect is included by using $\bar{\beta}_{\rm esc}$ and ${\rm e}^{-\tau}$ for the line and continuum absorption, respectively. For the line averaged escape probability $\bar{\beta}_{\rm esc}$, we use the fitting function given in Fukushima, Omukai & Hosokawa (2018), which depends on the column density $N_{\rm M}$ of molecular species M and the gas temperature T. The column density $N_{\rm M}$ is estimated from the local Jeans length as $N_{\rm M} = n_{\rm M}\lambda_{\rm J}$, where, $n_{\rm M}$ is the local number density of the species M. The effective continuum optical depth τ is given by the geometrical average of the Planck and Rosseland mean optical depths, $\tau = \sqrt{\tau_{\rm P}\tau_{\rm R}}$, where the Planck (Rosseland) mean optical depths $\tau_{\rm P(R)}$ are again estimated from those of the local Jeans length: $\tau_{\rm P(R)} = \kappa_{\rm P(R)}\rho\lambda_{\rm J}$. The Planck (Rosseland) mean opacity $\kappa_{\rm P(R)}$ are taken from Matsukoba et al. (2019). For the continuum cooling, we consider the H free–bound emission, H^- free–bound emission, H^- free–free emission, H free–free emission, H_2-H_2 collision-induced emission (CIE), and H_2-He CIE. The photon trapping effect is taken into account following Tanaka & Omukai (2014): the continuum cooling rate $\Lambda_{\rm cont}$ is given as

$$\Lambda_{\rm cont} = \frac{\Lambda_{\rm cont,thin}}{1 + \tau_{\rm P} + \frac{3}{4}\tau_{\rm R}\tau_{\rm P}}, \tag{10}$$

with the fitting function of optically thin case $\Lambda_{\rm cont,\,thin}$, which depends on the gas density and temperature from Matsukoba et al. (2019). The net chemical cooling rate $\Lambda_{\rm chem}$ is calculated by considering the H ionization/recombination and H_2 dissociation/formation:

$$\Lambda_{\rm chem} = \left(\chi_{\rm H} \frac{{\rm d}y({\rm H}^+)}{{\rm d}t} - \chi_{\rm H_2} \frac{{\rm d}y({\rm H_2})}{{\rm d}t} \right) n_{\rm H}, \tag{11}$$

where $\chi_{\rm H} = 13.6$ ev and $\chi_{\rm H_2} = 4.48$ ev are the binding energies, $y(i)$ is the chemical fraction of species i relative to the hydrogen nuclei, i.e. $y(i) = n(i)/n_{\rm H}$, with $n(i)$ and $n_{\rm H}$ the number density of species i and hydrogen nuclei, respectively.

We consider 20 chemical reactions among the nine species: H, H^+, H_2, e, H^-, H_2^+, D, HD, and D^+. We assume all the He is neutral with $y({\rm He}) = 9.722 \times 10^{-2}$. Table 1 shows the 20 chemical reactions selected from the minimal chemical reactions presented in Nakauchi et al. (2019). The reaction rate coefficients are also taken from Nakauchi et al. (2019). We solve the non-equilibrium chemistry at density $n_{\rm H} < 10^{18}$ cm^{-3}, but at higher density, set the chemical abundances to the equilibrium values since the chemical reaction time-scale is at least an order of magnitude smaller than free-fall time.

Table 1. Chemical reactions.

Number	Reaction
H1	$H^+ + e \rightleftharpoons H + \gamma$
H2	$H + e \rightleftharpoons H^- + \gamma$
H3	$H^- + H \rightleftharpoons H_2 + e$
H4	$H + H^+ \rightleftharpoons H_2^+ + \gamma$
H5	$H_2^+ + H \rightleftharpoons H_2 + H^+$
H6	$3H \rightleftharpoons H_2 + H$
H7	$2H_2 \rightleftharpoons 2H + H_2$
D1	$D + H^+ \rightleftharpoons D^+ + H$
D2	$D + H_2 \rightleftharpoons H + HD$
D3	$D^+ + H_2 \rightleftharpoons H^+ + HD$

Table 2. Model parameters.

Model	$E_{\rm r}/\lvert E_{\rm g}\rvert$	$E_{\rm m}/\lvert E_{\rm g}\rvert$	Ω_0 [s^{-1}]	B_0 [G]	μ_0
1.....	0	0	0	0	∞
2.....	0	2×10^{-5}	0	9.6×10^{-8}	270
3.....	0	2×10^{-3}	0	9.6×10^{-7}	27
4.....	0	2×10^{-1}	0	9.6×10^{-6}	2.7
5.....	0	9.5×10^{-1}	0	2.1×10^{-5}	1.2
6.....	10^{-6}	0	2.9×10^{-17}	0	∞
7.....	10^{-6}	2×10^{-5}	2.9×10^{-17}	9.6×10^{-8}	270
8.....	10^{-6}	2×10^{-3}	2.9×10^{-17}	9.6×10^{-7}	27
9.....	10^{-6}	2×10^{-1}	2.9×10^{-17}	9.6×10^{-6}	2.7
10....	10^{-4}	0	2.9×10^{-16}	0	∞
11....	10^{-4}	2×10^{-5}	2.9×10^{-16}	9.6×10^{-8}	270
12....	10^{-4}	2×10^{-3}	2.9×10^{-16}	9.6×10^{-7}	27
13....	10^{-4}	2×10^{-1}	2.9×10^{-16}	9.6×10^{-6}	2.7
14....	10^{-2}	0	2.9×10^{-15}	0	∞
15....	10^{-2}	2×10^{-5}	2.9×10^{-15}	9.6×10^{-8}	270
16....	10^{-2}	2×10^{-3}	2.9×10^{-15}	9.6×10^{-7}	27
17....	10^{-2}	2×10^{-1}	2.9×10^{-15}	9.6×10^{-6}	2.7

2.2 Initial conditions

We set the initial conditions following Machida et al. (2008c). As the initial density profile of cloud cores, we use the critical Bonnor–Ebert sphere (Ebert 1955; Bonnor 1956) $\rho_{\rm BE}(r)$, which is the isothermal sphere in hydrostatic equilibrium with external pressure. In order to promote a core collapsing, we increase the density profile by a factor $f = 1.4$. We also impose density fluctuations to induce the fragmentation during collapse:

$$\rho(r, \varphi) = \begin{cases} f\left[1 + \delta\rho(r, \varphi)\right]\rho_{\rm BE}(r) & \text{for } r < R_0, \\ f\left[1 + \delta\rho(r, \varphi)\right]\rho_{\rm BE}(R_0) & \text{for } r \geq R_0, \end{cases} \tag{12}$$

where the initial cloud radius $R_0 = 1.1 \times 10^6$ au. In this work, we assume a small m=2-mode density perturbation $\delta\rho$, such as,

$$\delta\rho(r, \varphi) = A_\varphi (r/R_0)^2 \cos 2\varphi, \tag{13}$$

where the amplitude $A_\varphi = 0.01$. Note that the initial density profile is uniquely determined by the central density and the isothermal tem-

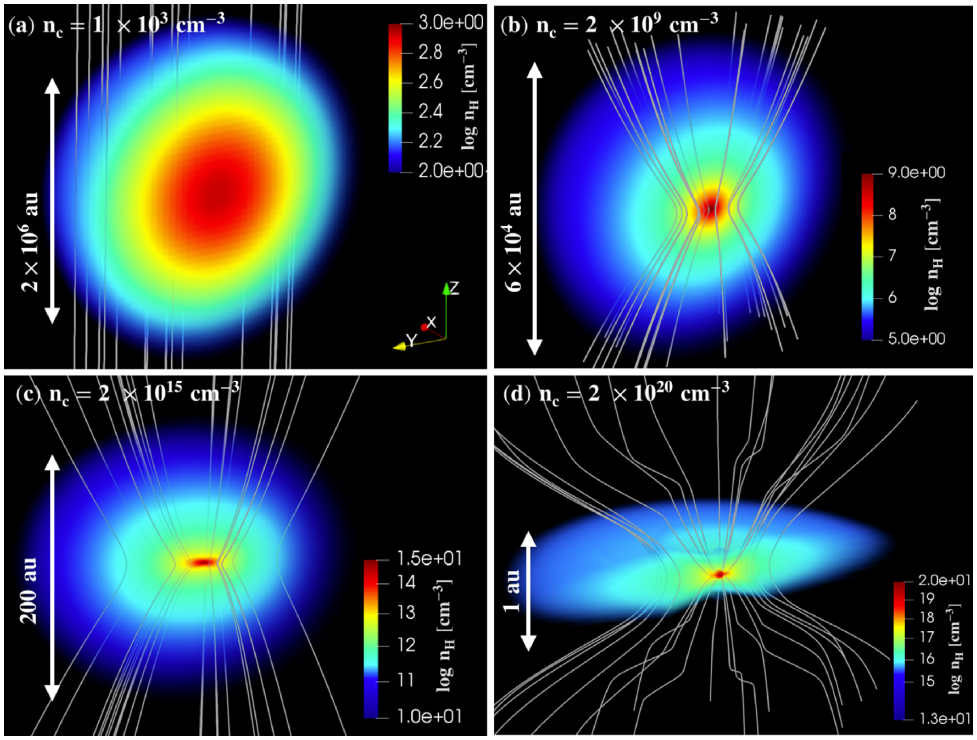

Figure 1. 3D volume rendering of the density field with the magnetic field lines for the non-rotating weak magnetic field model ($E_m/|E_g| = 2 \times 10^{-3}$). To make the central regions visible, only the density data on the rear side of the y–z plane ($x = 0$) is used for rendering. Each panel shows the cloud structure at four stages: the central density n_c = (a)1×10^3 cm^{-3}(initial state), (b) 2×10^9 cm^{-3}, (c) 2×10^{15} cm^{-3}, and (d) 2×10^{20} cm^{-3} (protostar formation).

perature, for which we adopt $\rho_{BE}(0) = 2.1 \times 10^{-21}$ g cm^{-3} (number density $n_{BE}(0) = 10^3$ cm^{-3}) and $T_{iso} = 198$ K. This temperature is taken from the value at the density $n_{BE}(0)f = 1.4 \times 10^3$ cm^{-3} obtained by the one-zone model of the cloud collapse with the same thermal and chemical processes. The total mass enclosed inside the initial radius R_0 is $M_c = 5.5 \times 10^3 M_\odot$ and the ratio of the gravitational energy to the thermal energy $\alpha = E_{th}/|E_g| = 0.6$.

We assume that the cloud is initially rigidly rotating around the z-axis with an angular velocity Ω_0 and pierced by a uniform magnetic field B_0 parallel to the rotation axis. As the boundary conditions, we also assume that both the magnetic fields and ambient gas outside the initial Bonner–Ebert sphere rotate at the initial angular velocity of the cloud (Matsumoto & Tomisaka 2004). The initial state is characterized with two parameters: the ratio of the rotational energy to the gravitational energy $E_r/|E_g|$ and that of the magnetic energy to the gravitational energy $E_m/|E_g|$. Table 2 summarizes the parameters of 17 models examined in this study. We also estimate the initial mass-to-flux ratio,

$$\left(\frac{M}{\Phi}\right) = \frac{M_c}{\pi R_0^2 B_0}, \tag{14}$$

where Φ denotes the magnetic flux. The dimensionless parameter μ_0 in Table 2 indicates the mass-to-flux ratio normalized by the critical value $(M/\Phi)_{cr}$ for a cloud with uniform density (Mouschovias & Spitzer 1976)

$$\left(\frac{M}{\Phi}\right)_{cr} = \frac{0.53}{3\pi}\left(\frac{5}{G}\right)^{\frac{1}{2}}. \tag{15}$$

3 RESULT

3.1 Evolution of non-rotating magnetized clouds

First, we study the evolution of non-rotating clouds to see magnetic field effects on the cloud deformation and suppression of the contraction. We then discuss how much the thermal evolution at the centre is affected by those effects. Weak and strong field cases are examined in Sections 3.1.1 and 3.1.2, respectively.

3.1.1 Weak field case

We here see the case with initial magnetic field strength $E_m/|E_g| = 2 \times 10^{-3}$, as an example of weak field cases. Fig. 1 shows the density and magnetic field structure at four stages: (a) the initial state with the central number density $n_c = 1 \times 10^3$ cm^{-3}, (b) 2×10^9 cm^{-3}, (c) 2×10^{15} cm^{-3}, and (d) 4×10^{20} cm^{-3}, corresponding to the protostar formation. Fig. 2 shows the equatorial (solid) and z-axial (dashed) profiles of (a) the density, (b) velocity, (c) temperature, and (d) H_2 abundance at the same stages shown in Fig. 1, where physical quantities on the equatorial plane are azimuthally averaged.

The initial state is the spherical core with $n_c = 1 \times 10^3$ cm^{-3} threaded by a weak uniform magnetic field (Fig. 1a). In early phases, the collapse is proceeding spherically, being unaffected by the weak field (Fig. 1b). Since the free-fall time-scale $t_{ff} \propto n_c^{-1/2}$ becomes shorter and shorter with increasing density, the central collapse proceeds in a runaway fashion with lower density surrounding region left behind. As a result, the collapsing cloud in this phase consists of a central core with a flat density distribution with the size of a local Jeans length and a lower density envelope with a power-law density distribution with the slope $\propto r^{-2.2}$ (green line in Fig. 2a). Note that this density slope is slightly steeper than that for the isothermal

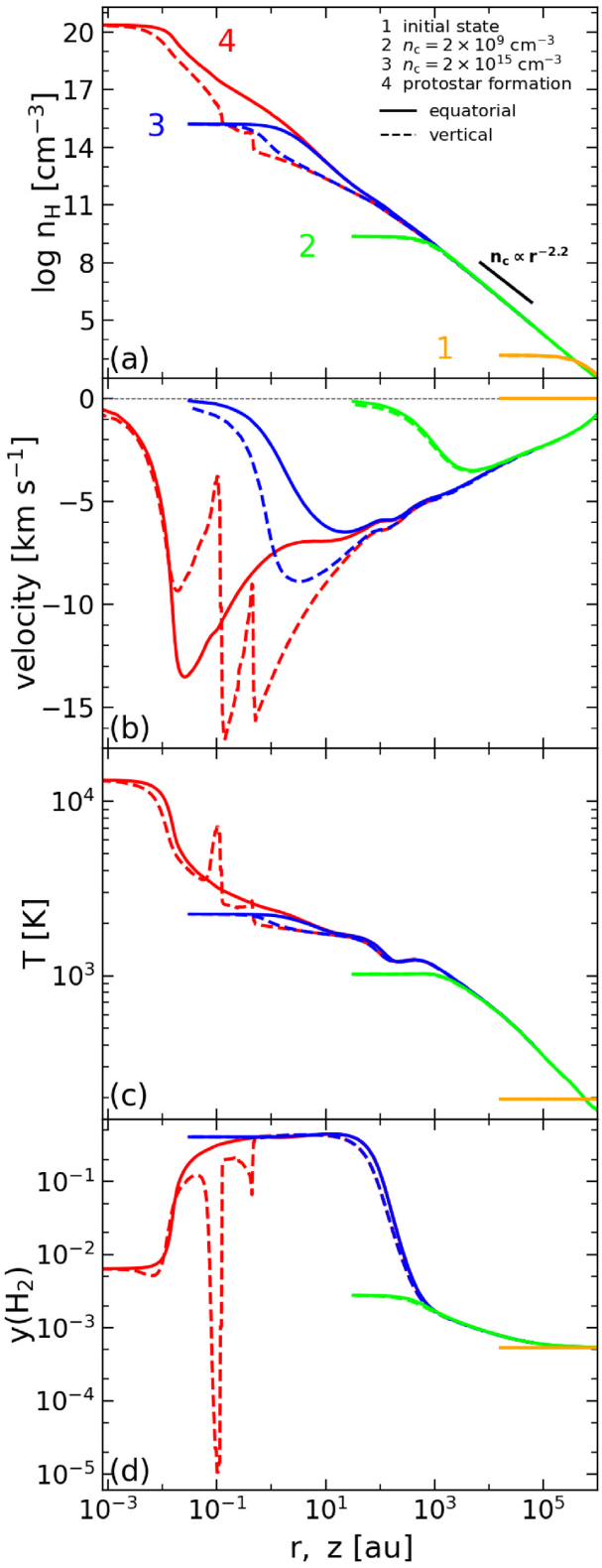

Figure 2. 1D gas profiles for the weak magnetic field model ($E_m/|E_g| = 2 \times 10^{-3}$) at the same stages as in Fig. 1, where physical quantities on the equatorial plane are azimuthally averaged. We provide the profiles of the (a) density, (b) velocity, (c) temperature, and (d) H_2 abundance in the equatorial (solid) and vertical (dashed) directions. In panel (b), the solid and dashed lines represent the equatorial and vertical velocities v_r and v_z, respectively. The yellow, green, blue, and red colours indicate the four stages of Figs 1(a)–(d), respectively.

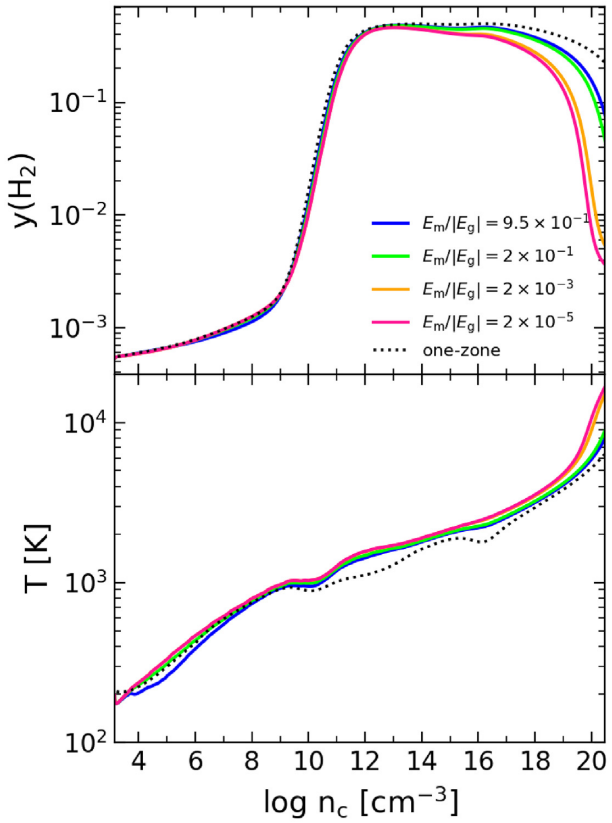

Figure 3. Evolution of the H_2 abundance (top) and temperature (bottom) of the core as a function of the central number density n_c. The non-rotating models with $E_m/|E_g| = 2 \times 10^{-5}$ (magenta), 2×10^{-3} (yellow), 2×10^{-1} (green), and 0.95 (blue) are shown. For comparison, the black dotted line is the temperature evolution obtained from the one-zone calculation.

collapse $\propto r^{-2}$ (Larson 1969; Penston 1969). Since the envelope density becomes $\propto r^{-2/(2-\gamma)}$ for the polytropic case $P \propto \rho^{\gamma}$ (Larson 1969; Yahil 1983), the density power index of -2.2 corresponds to $\gamma \simeq 1.1$ (Omukai & Nishi 1998).

Temperature evolution at the centre is shown in Fig. 3 (bottom panel) as a function of the density, along with those in cases with different magnetic field strength. The abundance of H_2, the dominant coolant in the primordial gas, is shown in the top panel of Fig. 3. We can see that the temperature increases gradually with the effective ratio of specific heat $\gamma \equiv \mathrm{d}(\ln p)/\mathrm{d}(\ln \rho) \simeq 1.1$ ($T \propto \rho^{0.1}$) before the formation of the adiabatic core, i.e. the protostar, at $\gtrsim 10^{20}$ cm^{-3}, as is expected from the envelope density structure in Fig. 2(a).

This thermal behaviour is controlled by H_2 chemistry that determines the cooling rate. The H_2 is first produced via the H^- channel with the abundance $\sim 5 \times 10^{-4}$ at $n_H \lesssim 10^3$ cm^{-3}. The effective ratio of specific heat $\gamma \simeq 1.1$ at $n_H = 10^3 - 10^9$ cm^{-3} is owing to the balance between the compressional heating and the H_2 cooling (bottom panel of Fig. 3). At higher densities $n_H \gtrsim 10^9$ cm^{-3}, the three-body H_2 formation reactions become effective and all the hydrogen is converted to the molecules at $n_H \sim 10^{12}$ cm^{-3} (top panel of Fig. 3). Although the cooling is enhanced due to the increased H_2 abundance, this is almost compensated by the chemical heating associated with the H_2 formation and the temperature decreases only slightly around $n_H \gtrsim 10^{10}$ cm^{-3}. At $n_H \gtrsim 10^{11}$ cm^{-3}, some H_2 lines become optically thick and the cooling rate gradually declines. At $n_H \sim 10^{13}$ cm^{-3} the temperature becomes high enough to dissociate some H_2 molecules and the dissociation cooling becomes important.

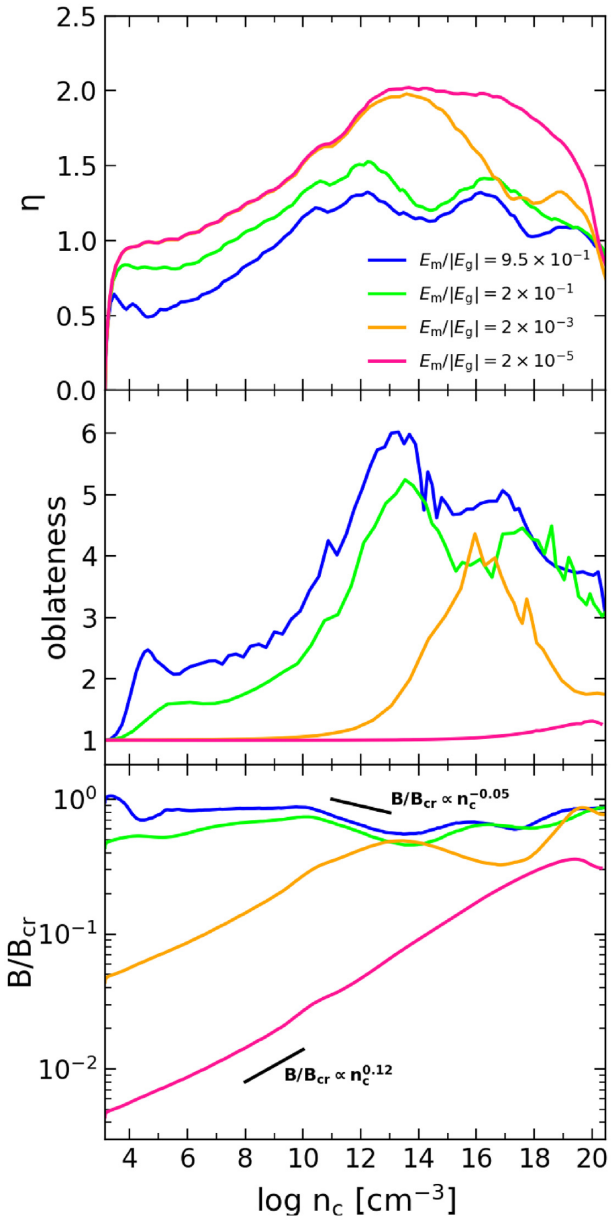

Figure 4. Same as Fig. 3, but for the collapse speed η (top), oblateness ϵ (middle), and magnetic field strength normalized by the critical value $B/B_{\rm cr}$ (bottom).

At somewhat higher densities $n_{\rm H} \sim 10^{15}$ cm^{-3}, the H_2 collision-induced emission (CIE) also plays some role in the cooling. Finally, at $n_{\rm H} \sim 10^{16}$ cm^{-3}, the central region becomes optically thick to the H_2 collision-induced absorption and the radiative cooling is strongly suppressed thereafter. At this time, rapid H_2 dissociation begins and associated cooling balances with the compressional heating until the completion of the dissociation. After that, a protostar forms at the centre, as we will explain in more detail later.

Starting with an initial weak field, the field becomes stronger as the field lines are gathered toward the centre by the gas contraction as seen in Fig. 1(b). The field strength at the centre is plotted in the bottom panel of Fig. 4 (yellow line for this model), where the field value is normalized by the critical magnetic field $B_{\rm cr}$, i.e. the field value required for the magnetic force to balance the gravity: if the magnetic field reaches the critical value, the collapse will be stopped by the magnetic force. Here the critical magnetic field $B_{\rm cr}$ is calculated from the balance between the magnetic force ($\propto (\nabla \times \boldsymbol{B}) \times \boldsymbol{B}$) and gravity acting on a uniform density core with the Jeans size, and is given by

$$B_{\rm cr} = \sqrt{\frac{4\pi G M_{\rm J} \rho_{\rm c}}{R_{\rm J}}}, \tag{16}$$

where $M_{\rm J}$, $R_{\rm J}$ and $\rho_{\rm c}$ are the Jeans mass, Jeans radius and central mass density, respectively. Note that $B_{\rm cr} \propto \sqrt{n_{\rm c} T}$ as $R_{\rm J} \propto \sqrt{T/n_{\rm c}}$ and $M_{\rm J} \propto R_{\rm J}^3 n_{\rm c}$. In the case of spherical collapse, a magnetic field increases as $B \propto n_{\rm c}^{2/3}$. To drive this relation, a uniform magnetic field B and uniform density $\rho_{\rm c}$ (or $n_{\rm c}$) are assumed within the cloud radius $R_{\rm c}$. Then we consider the spherical collapse with mass and magnetic flux conservation ($\rho_{\rm c} R_{\rm c}^3 = $ const., $B R_{\rm c}^2 = $ const.). In this case, the magnetic field increases with decreasing cloud radius $R_{\rm c}$ as $B \propto R_{\rm c}^{-2}$ while the density increases as $n_{\rm c} \propto R_{\rm c}^{-3}$. Therefore, the relation between B and $n_{\rm c}$ is given as $B \propto n_{\rm c}^{2/3}$. If we write $B \propto n_{\rm c}^{\alpha}$, with the shape parameter α ($\alpha = 2/3$ for the spherical collapse, as we have seen above), the ratio B and $B_{\rm cr}$ is given by $B/B_{\rm cr} \propto n_{\rm c}^{\alpha - \gamma/2}$ for $T \propto n_{\rm c}^{\gamma - 1}$. Substituting $\alpha = 2/3$ for the spherical collapse and $\gamma = 1.1$ for the primordial gas, we obtain the relation $B/B_{\rm cr} \propto n_{\rm c}^{0.12}$, shown by the thick black line in the bottom panel of Fig. 4. As seen in this figure, the magnetic field grows monotonically along this slope in a weak field case (yellow line), which indicates the collapse proceeds spherically.

As the field strength approaches the critical value, magnetic effects become apparent in two ways, suppression of the contraction and deformation of the cloud. To see the effect on the contraction, in the top panel of Fig. 4, we show the collapse speed at the centre with respect to the free-fall time, $\eta = t_{\rm ff}/t_{\rm dyn}$, where $t_{\rm dyn} = \rho_{\rm c}/\dot{\rho}_{\rm c}$ is the time-scale of the actual central contraction on the simulation, and $t_{\rm ff} = \sqrt{3\pi/(32 G \rho_{\rm c})}$ is the free-fall time. For the free-fall collapse with no pressure effect, the collapse speed asymptotically reaches $\eta = 3\pi/2 = 4.7$, whereas for the Larson–Penston similarity solution (Larson 1969; Penston 1969), which describes dynamical collapse of an isothermal cloud, it gives $\eta = 3.0$. Omukai, Hosokawa & Yoshida (2010) have found η reaches $\simeq 2.5$ during the pre-stellar collapse of the primordial gas from one-dimensional hydrodynamical calculation. In Fig. 4, the collapse speed for the case with the weakest field ($E_{\rm m}/|E_{\rm g}| = 2 \times 10^{-5}$, magenta line) is unaffected by the magnetic force throughout the collapse. The difference in η from this curve thus shows the delay due to the magnetic force. In the case currently discussed ($E_{\rm m}/|E_{\rm g}| = 2 \times 10^{-3}$, yellow), the magnetic field does not affect the collapse speed below $n_{\rm c} \sim 10^{12}$ cm^{-3}, but it begins to delay the collapse once $B/B_{\rm cr}$ reaches $\simeq 0.4$ at $n_{\rm c} \sim 10^{12}$ cm^{-3}.

Simultaneously the cloud shape is deformed by the magnetic force. To see the degree of deformation, we plot the oblateness of the core ϵ in the middle panel of Fig. 4. The oblateness is defined as $\epsilon = \sqrt{L_x L_y}/L_z$, where L_x, L_y, L_z are the x, y, z axis lengths from the centre to the surface where the density is one-tenth of the central value. In the model with $E_{\rm m}/|E_{\rm g}| = 2 \times 10^{-3}$ (yellow), the cloud keeps spherical shape early on ($\epsilon \simeq 1$), and begins to become oblate at $n_{\rm c} \sim 10^{12}$ cm^{-3}. Density and magnetic field structure of the deformed cloud at $n_{\rm c} = 2 \times 10^{15}$ cm^{-3} is shown in Fig. 1(c). As the magnetic force acts mainly on the direction perpendicular to the field lines, the contraction is more suppressed in the equatorial rather than in the z-axial direction. This can be seen in the difference between the equatorial and vertical velocity, i.e. $|v_r| < |v_z|$ (Fig. 2b, blue line). The cloud eventually becomes very oblate, disc-like shape. The cloud deformation slows down the field growth and $B/B_{\rm cr}$ even decreases with $\propto n_{\rm c}^{-0.05}$ when the centre

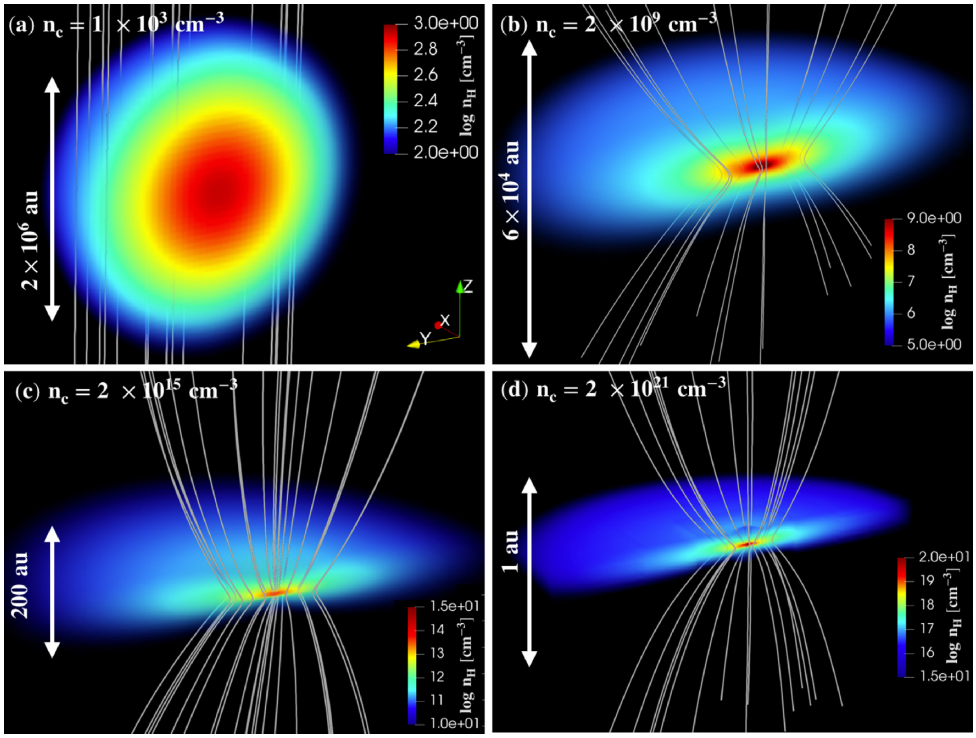

Figure 5. Same as Fig. 1, but for the non-rotating strong magnetic field model ($E_m/|E_g| = 0.95$). The central density for panel (d), corresponding to the protostar formation, is 2×10^{21} cm^{-3}.

density reaches $n_c \simeq 10^{13}$ cm^{-3}(bottom panel of Fig. 4, yellow line). This approximately corresponds to the sheet-like contraction with a scale height $H = c_s/\sqrt{G\rho_c}$, where c_s is the sound speed. In such a case, we can get $B \propto n_c^{1/2}$ from $B \propto R_c^{-2}$ (flux conservation) and $n_c \propto R_c^{-4}$ (mass conservation: $n_c R_c^2 H =$ const.). In other words, when the cloud is sheet-like, suppression of the collapse by the magnetic field becomes weaker as the collapse proceeds. As a result, magnetic force does not completely stop the contraction.

The cloud structure at protostar formation is shown in Fig. 1(d). We can see a disc-like structure around the protostar. This is a pseudo-disc, which is supported by anisotropic magnetic tension, rather than by rotation (Galli & Shu 1993). Around the surface of the pseudo-disc, the motion in the z direction suddenly decelerated at the shocks located around $z \simeq 0.1$ and 0.6 au (Fig. 2b, red line). As a result, these shocks heat up the gas (Fig. 2c, red line). Since the shock suppresses the contraction in the z direction, v_r becomes larger than v_z at $z \simeq 0.1$ au (Fig. 2b). The contraction proceeds only in the equatorial direction with the height in the z direction kept constant. In such a case, we obtain $B \propto n_c$ from $B \propto R_c^{-2}$ (flux conservation) and $n_c \propto R_c^{-2}$ (mass conservation). This allows the magnetic field to grow again towards the critical value B_{cr} at $n_c \sim 10^{18}$ cm^{-3} (yellow line in bottom panel of Fig. 4).

When the density reaches $n_c \sim 10^{19}$ cm^{-3} at the centre, molecular hydrogen is rapidly dissociated due to high temperature, with its abundance falling below 10^{-2} (yellow line in top panel of Fig. 3). The dissociation being almost completed, the temperature increases adiabatically, i.e. $\gamma > 4/3$ thereafter (yellow line in bottom panel of Fig. 3). As a result, increasing thermal pressure overcomes the gravity and a hydrostatic core, or i.e. a protostar, is formed at the centre. The protostar has mass $M_p = 2.6 \times 10^{-3}\,M_\odot$ and radius in the x–y plane $r_p = 1.4 \times 10^{-2}$ au. In our analysis, we have defined a protostar as a core whose central density is greater than 10^{20} cm^{-3} and H_2 abundance is less than 10^{-2}.

3.1.2 *Strong field case*

Next, we see the case of a cloud with an initial strong magnetic field comparable to the gravity, i.e. $E_m/|E_g| = 9.5 \times 10^{-1}$. Fig. 5 shows the three-dimensional structure of density and magnetic field lines at four evolutionary stages, as in Fig. 1. Fig. 6 shows the profiles of (a) density, (b) velocity, (c) temperature, and (d) H_2 abundance for the same four stages.

Since the initial field is already close to the critical value B_{cr} (blue line in the bottom panel of Fig. 4), magnetic field effects are visible soon after the onset of collapse. The collapse remains slow with $\eta =$ 0.5–0.6 until $n_c \sim 10^8$ cm^{-3} (blue line of the top panel of Fig. 4). This slower collapse and thus lower compressional heating result in lower temperature than in the cases with weaker field (Fig. 3, bottom) although the temperature difference is only modest due to high temperature sensitivity of the H_2 cooling rate.

Also the cloud shape immediately becomes oblate with $\epsilon \simeq 2$ by the strong magnetic force (blue line in the middle panel of Fig. 4) and thus the disc-like structure forms earlier than weaker field cases. Such shape evolution can be also seen in Fig. 5. As a result of the deformation, the field strength remains at $B/B_{cr} \simeq 0.6$–0.8 despite the contraction, as discussed in Section 3.1.1 (blue line in the bottom panel of Fig. 4).

When the density reaches $n_c \sim 10^{15}$ cm^{-3} (Fig. 5c), the collapse speed is still 1.7 times slower than in the weakest field cases ($E_m/|E_g| = 2 \times 10^{-5}$) due to the magnetic force (top panel of Fig. 4). As a result, the strong field reduces the compressional heating without changing the H_2 CIE cooling rate and the temperature becomes slightly lower compared with the weaker field cases (bottom panel of Fig. 3). This results in later onset of the H_2 dissociation and slightly higher H_2 abundance (upper panel of Fig. 3). Consequently the strong magnetic field raises the density at which the protostar forms due to the delayed H_2 dissociation (Figs 2a and 6a). The stage

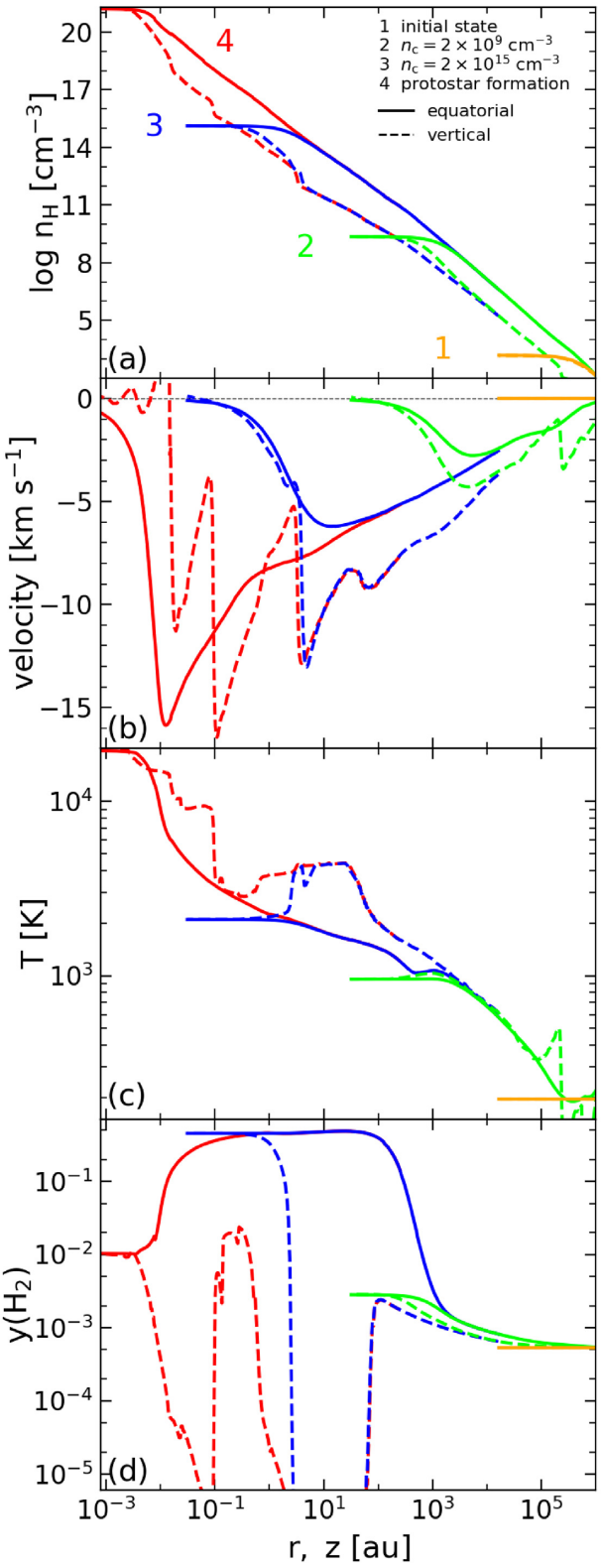

Figure 6. Same as Fig. 2, but for the non-rotating strong magnetic field model ($E_m/|E_g| = 0.95$). The colours correspond to the four epochs in Fig. 5.

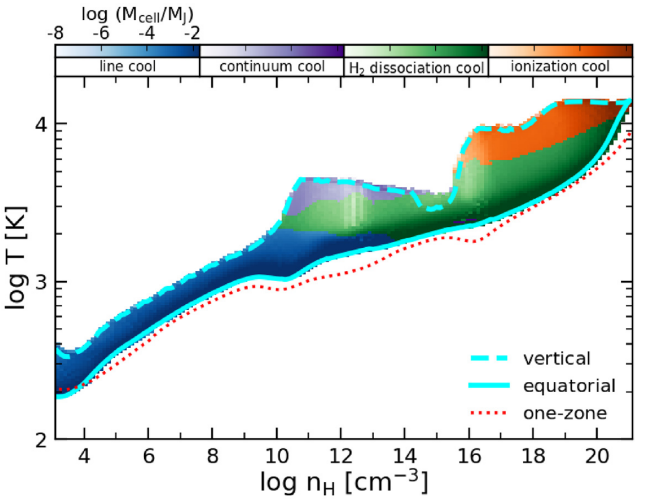

Figure 7. Density–temperature distribution at the epoch of protostar formation in the n–T plane for the strong magnetic field model ($E_m/|E_g| = 0.95$). The blue, purple, green, and orange colours represent the region dominated by line cooling, continuum cooling, H_2 dissociation cooling, and ionization cooling, respectively. Each colour scale indicates the concentration of mass, the cell mass M_{cell} normalized by Jeans mass M_J, in each bin. The solid and dashed lines represent the temperature profile in the equatorial and vertical directions. For comparison, the red dotted line is the temperature obtained from the one-zone calculation.

of the protostar formation is shown in Fig. 5(d), and we can see the protostellar surface at $r,\ z = 0.01$ au from the velocity profile (red line in Fig. 6b).

Fig. 7 shows the density–temperature distribution at the same stage as in Fig. 5(d) in the n–T plane. The blue, purple, green and orange colours represent the region dominated by line cooling, continuum cooling, H_2 dissociation cooling and ionization cooling, respectively. The solid and dashed lines indicate the equatorial (x–y plane) and vertical (z-axis) temperature profiles. From this figure, we can see that the temperature in regions above the mid-plane is higher than the one-zone calculation (red dotted line). This is caused by the high compressional heating rate and the shock heating around the pseudo-disc. The first ($n_H \sim 10^{10}$ cm^{-3}) and second ($n_H \sim 10^{16}$ cm^{-3}) bumps in Fig. 7 correspond to the shocks at $z \simeq 63$ and 0.1 au, respectively (Fig. 6b). The temperature at the lower density shock is limited by the continuum cooling, especially, the H^- free–bound cooling, while that at higher density is limited by the ionization cooling. This result indicates that the temperature in the outer part can be significantly changed by the cloud deformation due to magnetic forces.

In summary, magnetic force delays the collapse, as well as changes the cloud shape. The latter effect prevents the field from reaching the critical value B_{cr} and stopping the collapse. As a result, the change in the temperature evolution due to the delayed collapse remains small at the cloud centre even in cases with a strong field. On the other hand, pseudo-disc formation by the magnetic force causes shocks near the disc surface, and associated heating significantly modifies the surrounding temperature structure (Fig. 6c or Fig. 7).

3.2 Cases both with rotation and magnetic field

In this section, we see the cases of rotating and magnetized clouds. Without magnetic fields, the angular momentum is not transported from the core during axisymmetric collapse. Eventually, the centrifugal force balances with the gravity and the disc or ring-like structure

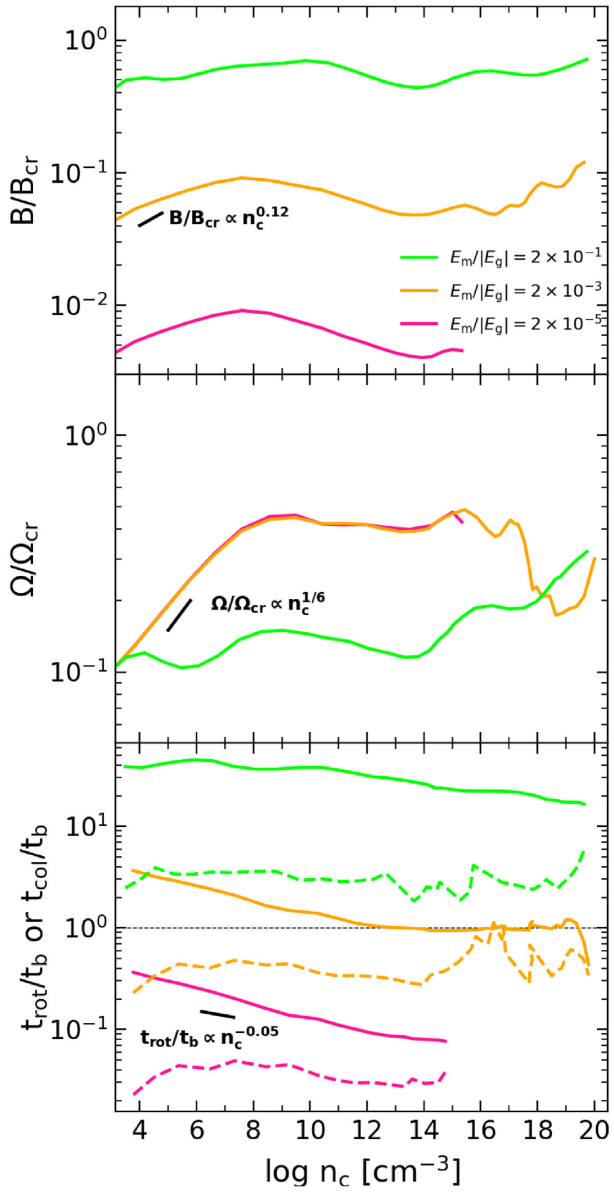

Figure 8. Evolution of the magnetic field normalized by the critical value $B/B_{\rm cr}$ (top) and angular velocity normalized by the Keplerian value $\Omega/\Omega_{\rm cr}$ (middle) of the core as a function of the central number density $n_{\rm c}$. The rotating models with $E_{\rm r}/|E_{\rm g}| = 1 \times 10^{-2}$ and $E_{\rm m}/|E_{\rm g}| = 2 \times 10^{-5}$ (magenta), 2×10^{-3} (yellow), and 2×10^{-1} (green) are shown. At the bottom, we also plot the time-scale ratios $t_{\rm rot}/t_{\rm b}$ (solid) and $t_{\rm col}/t_{\rm b}$ (dashed), where $t_{\rm rot}$, $t_{\rm col}$, and $t_{\rm b}$ are the rotational, collapse, and magnetic braking time-scale, respectively.

is formed at the centrifugal radius. However, magnetic fields, if exist, can efficiently transport angular momentum. For example, in the so-called magnetic braking, the field lines twisted by rotation brake the rotational motion by magnetic tension (e.g. Mouschovias & Paleologou 1979). Also the magnetic field can launch MHD winds from a rotating cloud, thereby also extracting the angular momentum (Blandford & Payne 1982). We here investigate the effects of the magnetic braking and MHD outflow on the collapsing cloud.

We show the collapse of the cloud with initial rotational energy $E_{\rm r}/|E_{\rm g}| = 1 \times 10^{-2}$ as an example where rotation effects can be seen clearly. Note that first-star-forming clouds have rotational energy about $E_{\rm r}/|E_{\rm g}| = 10^{-2}$–$10^{-1}$ according to the cosmological simulation (e.g. Hirano et al. 2014). Models with different rotational energy will be discussed in Section 3.3.

To see the importance of magnetic and centrifugal forces, we show in Fig. 8 the magnetic field normalized by the critical value $B/B_{\rm cr}$ (top panel) and the angular velocity Ω normalized by the Keplerian value $\Omega_{\rm cr}$ (middle panel) for the models with different initial magnetic field strength $E_{\rm m}/|E_{\rm g}| = 2 \times 10^{-5}, 2 \times 10^{-3}$, and 2×10^{-1}. We define the Keplerian angular velocity $\Omega_{\rm cr}$ as

$$\Omega_{\rm cr} = \sqrt{\frac{4\pi G\bar{\rho}}{3}}, \tag{17}$$

where $\bar{\rho}$ is the average density inside the core, defined as $\rho > \rho_{\rm c}/10$.

For later convenience, we describe the increase of angular velocity with density as $\Omega \propto n_{\rm c}^{\alpha}$, with the index α depending on the cloud shape. The value of α can be obtained from the mass and angular momentum conservation: $\alpha = 2/3$ (1/2) for the spherical (sheet-like, respectively) case. Note that this dependence is the same as that of the magnetic field described in Section 3.1. Thus, we can get the relation $B/B_{\rm cr} \propto n_{\rm c}^{\alpha-\gamma/2}$ (Section 3.1) and $\Omega/\Omega_{\rm cr} \propto n_{\rm c}^{\alpha-1/2}$.

In the weak field cases of $E_{\rm m}/|E_{\rm g}| = 2 \times 10^{-5}$ and 2×10^{-3}, early collapse proceeds spherically unaffected either by the magnetic force or rotation. Therefore, $B/B_{\rm cr}$ and $\Omega/\Omega_{\rm cr}$ grow monotonically with the slope corresponding to $\alpha = 2/3$ (top and middle panels in Fig. 8). By the time the central density reaches 10^8 cm^{-3}, the rotation velocity grows to $\Omega/\Omega_{\rm cr} \simeq 0.4$, and the centrifugal force begins to affect the collapse. On the other hand, the magnetic field is still weak and has little effect. In those cases, the cloud becomes oblate solely by the rotation effect at the density $n_{\rm c} \sim 10^8$ cm^{-3}. After that, $B/B_{\rm cr}$ and $\Omega/\Omega_{\rm cr}$ evolve with the slope corresponding to $\alpha \sim 1/2$ (Fig. 8). In contrast, for the strong field model ($E_{\rm m}/|E_{\rm g}| = 2 \times 10^{-1}$), the magnetic field remains around $B/B_{\rm cr} \lesssim 1$ throughout the collapse. Due to the strong field, the cloud becomes disc-like soon after the onset of the collapse. In addition, the rotation is suppressed by the magnetic braking. By the combination of the disc-like collapse and magnetic braking, the rotation velocity remains slow, and the centrifugal force is weaker than either gravity or magnetic forces throughout the collapse.

The magnetic braking significantly affects the rotation velocity in the strong field case. To see when it operates, we compare three time-scales: the collapse time-scale $t_{\rm col} = 3\rho_{\rm c}/\dot{\rho}_{\rm c}$, rotation time-scale $t_{\rm rot} = 2\pi/\Omega$, and angular momentum transfer time-scale by the magnetic braking $t_{\rm b} = R_{\rm J}/v_{\rm A}$, where $v_{\rm A}(= B/\sqrt{4\pi\rho_{\rm c}})$ is Alfven velocity at the centre, respectively. If $t_{\rm b}$ becomes shorter than $t_{\rm col}$, the magnetic braking effectively transports the angular momentum during the collapse. In the bottom panel of Fig. 8, we plot the ratio $t_{\rm rot}/t_{\rm b}$ (solid) and $t_{\rm col}/t_{\rm b}$ (dashed) of the average values inside the core for each model. In the strong field case ($E_{\rm m}/|E_{\rm g}| = 2 \times 10^{-1}$, green line), $t_{\rm col}/t_{\rm b} > 1$ from the beginning. Thus, the angular momentum is extracted from the centre soon after the collapse begins. In contrast, in the weaker field cases with $E_{\rm m}/|E_{\rm g}| = 2 \times 10^{-3}$ (yellow line) and 2×10^{-5} (magenta line), $t_{\rm col}/t_{\rm b} < 1$ and the braking time-scale is longer than the collapse time-scale. It means the collapse significantly proceeds before the angular momentum is transported by the magnetic braking. We can also see the effect of the magnetic braking in the behaviour of $t_{\rm rot}/t_{\rm b}$. Here, $t_{\rm b}$ can be written as $t_{\rm b} \sim R_{\rm J}/v_{\rm A} \sim (c_{\rm s}/v_{\rm A})t_{\rm ff} = (B_{\rm cr}/B)t_{\rm ff}$, where we use the relation $B_{\rm cr} = (4\pi k_{\rm b} n_{\rm c} T)^{1/2} = (4\pi\rho_{\rm c})^{1/2} c_{\rm s}$. For conserved magnetic flux, $B/B_{\rm cr} \propto n_{\rm c}^{\alpha-\gamma/2}$ (Section 3.1) and $t_{\rm b} \propto n_{\rm c}^{(\gamma-1)/2-\alpha}$, while, for conserved angular momentum, $t_{\rm rot} = 2\pi/\Omega \propto n_{\rm c}^{-\alpha}$. Therefore the ratio $t_{\rm rot}/t_{\rm b}$ is given as $t_{\rm rot}/t_{\rm b} \propto n_{\rm c}^{(1-\gamma)/2}$, which depends only on the temperature evolution, i.e. the effective ratio of specific heat γ and is independent of the cloud shape factor α. For the primordial gas

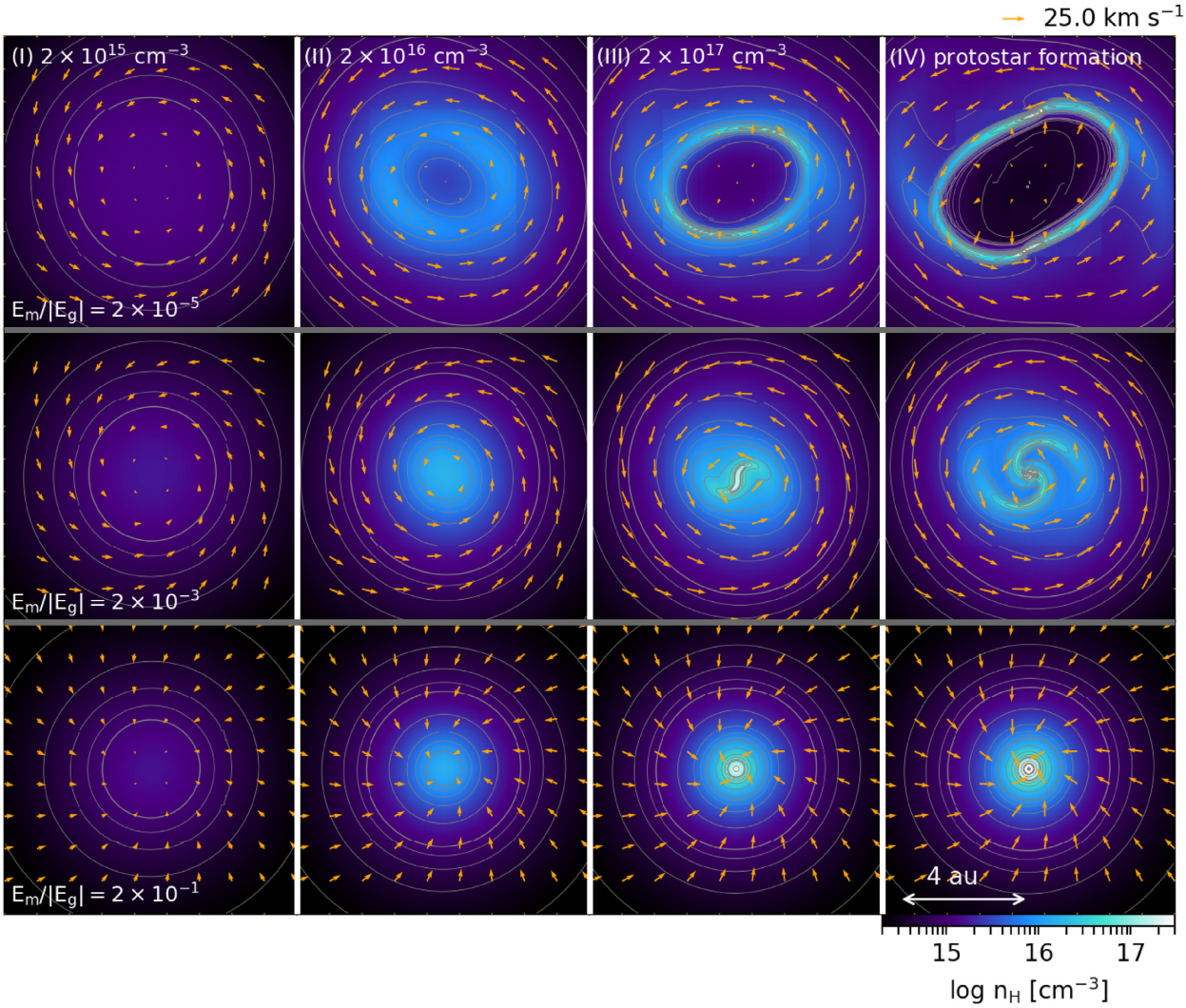

Figure 9. Face-on sliced density distributions at four late stages for the rotating models with $E_r/|E_g| = 1 \times 10^{-2}$ and $E_m/|E_g| = 2 \times 10^{-5}$ (top), 2×10^{-3} (middle), and 2×10^{-1} (bottom). The first three columns correspond to the stages when the central density $n_c =$ (I) 2×10^{15} cm^{-3}, (II) 2×10^{16} cm^{-3}, and (III) 2×10^{17} cm^{-3}, with the last column for (IV) just after the protostar formation. Orange arrows in each snapshot represent the projected velocity. The thin lines represent the density contours.

($\gamma \simeq 1.1$), this slope is -0.05 for conserved angular momentum. The slope less steeper than -0.05 indicates the angular momentum loss due to the magnetic braking. In the bottom panel of Fig. 8, we can see that the slope in the weak field cases with $E_m/|E_g| = 2 \times 10^{-5}$ and 2×10^{-3} is indeed -0.05, while the slope in the strong field case with $E_m/|E_g| = 2 \times 10^{-1}$ is flatter owing to the magnetic braking.

Next we see the evolution in the late collapse phase with $n_c > 10^{15}$ cm^{-3}, where difference in the cloud structure becomes apparent among the models. Fig. 9 shows the cloud structure in this phase for the cases with $E_m/|E_g| = 2 \times 10^{-5}$ (top), 2×10^{-3} (middle), and 2×10^{-1} (bottom). For each model, we show the snapshots of face-on sliced density (x–y plane) at $n_c =$ (I) 2×10^{15} cm^{-3}, (II) 2×10^{16} cm^{-3}, (III) 2×10^{17} cm^{-3}, and (IV) just after protostar formation. The orange arrows in each panel represent the velocity vectors projected on to the x–y plane. The snapshots on the x–z plane at the same epochs are shown in Fig. 10. The density distribution is shown in the upper half of each panel while the temperature distribution in the lower half. We enclosed the regions where the velocity in the z direction is outward, i.e. the outflow regions by white lines. The final snapshot (panel IV) is taken at 20 days after the protostar formation because further calculations require large computational cost.

The dependence on the magnetic field strength is apparent in the late collapse phase. In stage (I), we can see the axisymmetric discs in all three cases. In the cases with $E_m/|E_g| = 2 \times 10^{-5}$ and 2×10^{-3}, the disc is rotationally supported, while, in the strong field case with $E_m/|E_g| = 2 \times 10^{-1}$, it is magnetically supported. This difference is reflected in the velocity field: rotating spiral motions are obvious in the weak field cases, whereas the gases are moving toward the centre with little rotation in the strong field case. Difference in the magnetic field strength and thus the angular momentum extraction via the magnetic braking significantly changes the density structure. In the case with $E_m/|E_g| = 2 \times 10^{-5}$ (top panel), where the angular momentum is roughly conserved due to ineffective magnetic braking (see $t_{col}/t_b, t_{rot}/t_b \ll 1$ in bottom panel of Fig. 8), a ring is formed at $n_c \simeq 1 \times 10^{15}$ cm^{-3}. The ring is gravitationally unstable, and immediately breaks into two fragments (Fig. 9, top panel III). Each fragment collapses until $n_c \simeq 8 \times 10^{20}$ cm^{-3}, with their separation

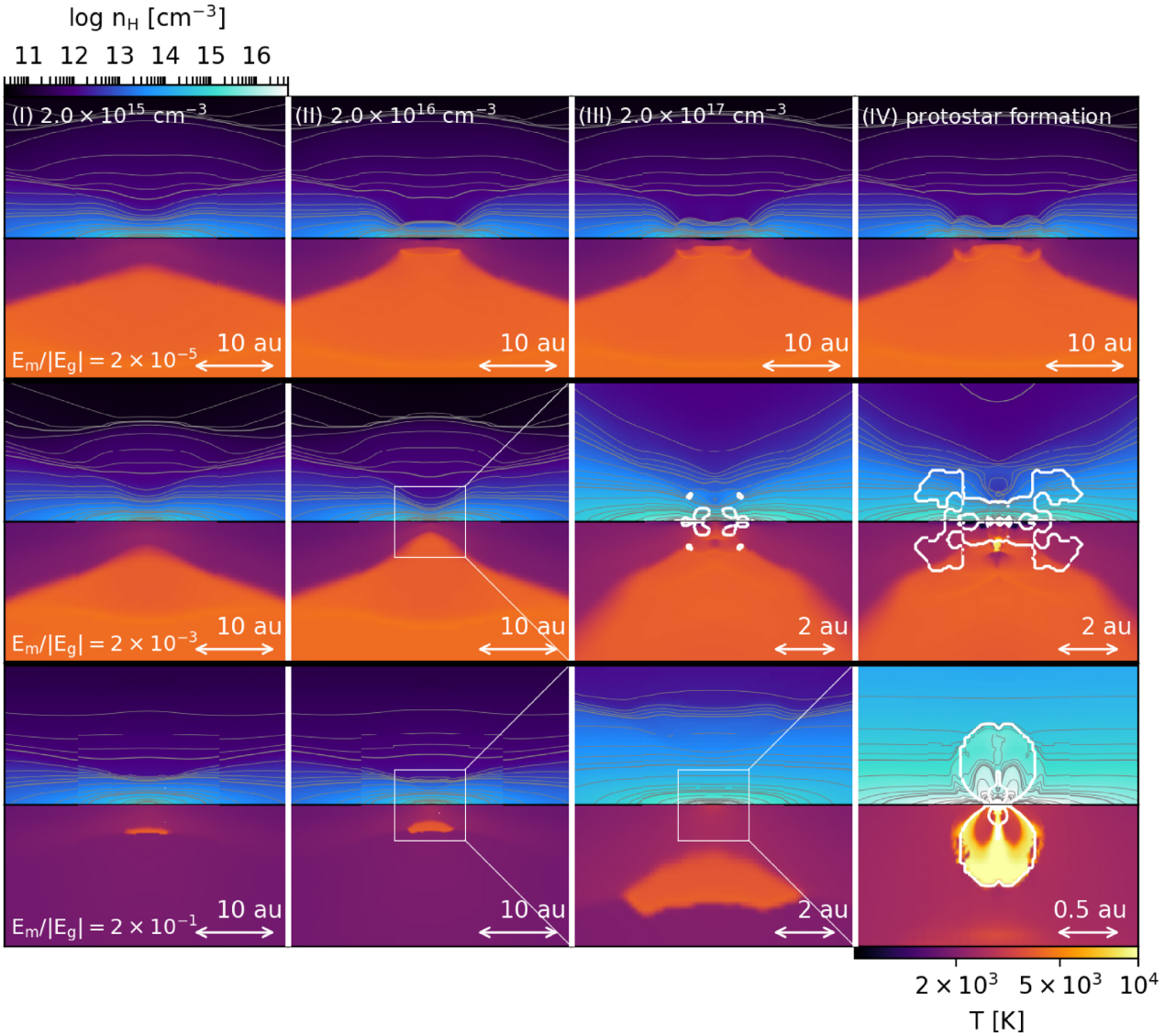

Figure 10. Same as Fig. 9, but for the edge-on sliced density and temperature distributions, which are shown in the upper and lower halves of each panel, respectively. Thick white contours indicate the outflow regions where the z-component of the velocity is outward. The thin lines in the upper half of each panel represent the density contours.

about 5 au. In the stronger field case with $E_m/|E_g| = 2 \times 10^{-3}$, the magnetic time-scale t_b satisfies the condition $t_{rot}/t_b \gtrsim 1$ until the rotation motion slows down the collapse at $n_c \simeq 1 \times 10^{15}$ cm^{-3} (Fig. 8 bottom). This means that the magnetic braking significantly slows down the rotation. As a result, we observe the formation of spiral arms instead of a ring at the stage (III). The central part further contracts and a protostar is formed at $n_c \simeq 2 \times 10^{20}$ cm^{-3} with the radius 4×10^{-2} au. In the strongest field case with $E_m/|E_g| = 2 \times 10^{-1}$, rotational motion is strongly suppressed by the magnetic braking and spherical collapse continues (Fig. 9, bottom) until the protostar formation at stage (IV) with the radius 4×10^{-2} au. In summary, the strong magnetic field efficiently extracts angular momentum, thereby suppressing fragmentation during the collapse.

Finally, we investigate the outflow from the central region. Fig. 11 shows the density and magnetic field structure just after protostar formation (stage IV in Fig. 10), where the outflow region is indicated by purple surface for the cases with $E_m/|E_g| = 2 \times 10^{-5}, 2 \times 10^{-3}$, and 2×10^{-1}. In the cases with $E_m/|E_g| \geq 2 \times 10^{-3}$, the outflows are launched due to the field lines twisted by the rotational motion. In the strongest field case with $E_m/|E_g| = 2 \times 10^{-1}$, rotational motion begins to dominate during the protostar formation and generates a toroidal magnetic field (B_r, B_ϕ), which launches the outflow (bottom panel of Fig. 11) with the maximum velocity $v_{max} = 40$ km s^{-1}, in the same order of magnitude as the escape velocity. In the moderate case with $E_m/|E_g| = 2 \times 10^{-3}$, a rotating disc emerges during the collapse and outflows are launched (middle row at stage III of Fig. 10) with slower velocity ($v_{max} = 16$ km s^{-1}) owing to the shallower gravitational potential of the launching points than in the former case. No outflow is observed in the weakest field case with $E_m/|E_g| = 2 \times 10^{-5}$. Because of very weak magnetic force, the field lines are dragged by the rotational motion, resulting in a toroidal field with a configuration almost parallel to the disc $B_z, B_r \ll B_\phi$ (top panel of Fig. 11). Magneto-centrifugal winds cannot be launched by this kind of field configuration since the centrifugal force is almost perpendicular to the field lines. If we extend the calculation until later time, however, the field could be further amplified by rotation

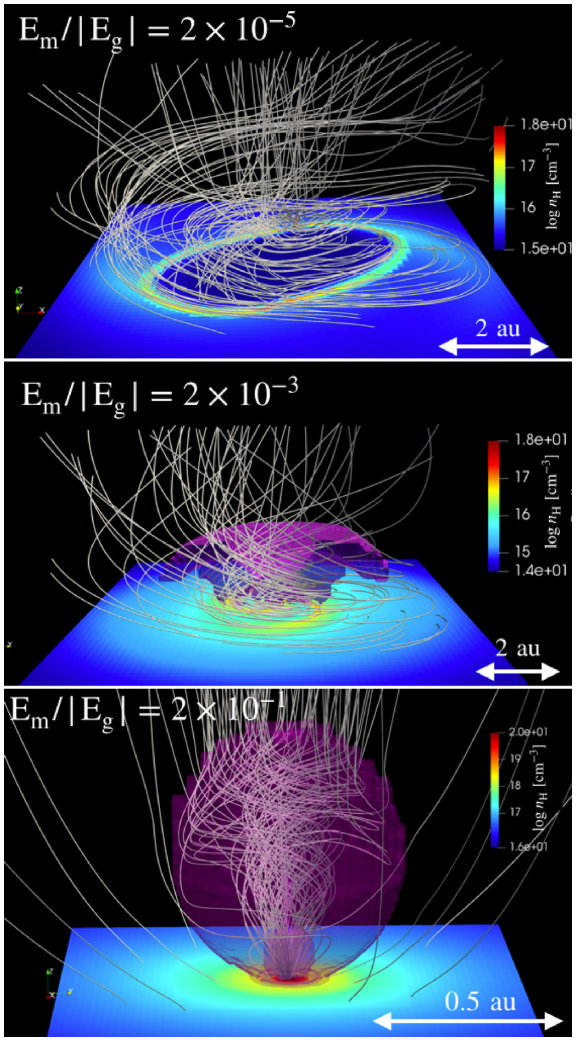

Figure 11. 3D structure of magnetic field lines along with the sliced equatorial density distributions just after the protostar formation. We show the snapshots for the rotating models with $E_r/|E_g| = 1 \times 10^{-2}$ and $E_m/|E_g| = 2 \times 10^{-5}$ (top), 2×10^{-3} (middle), and 2×10^{-1} (bottom). The purple surfaces indicate the outflow regions.

of the disc. In such a case, another mechanism of MHD winds, called magnetic-pressure-driven wind (e.g. Blandford & Payne 1982; Tomisaka 2002; Machida, Inutsuka & Matsumoto 2008a), might be eventually launched.

In our simulations, the amount of angular momentum transferred by the outflow is smaller than that by the magnetic braking since the outflows are launched only in a late phase of the protostar formation. Also in the present-day star formation, the angular momentum is mainly removed by magnetic braking.(e.g. Marchand et al. 2020). We thus expect that the magnetic braking plays a more important role in controlling fragmentation of first-star-forming clouds.

3.3 Fragmentation and outflow conditions

3.3.1 Fragmentation conditions

First, we discuss the fragmentation condition. The density structure on the x–y plane just after the protostar formation is shown in Fig. 12 for models with different initial field strength $E_m/|E_g|$ and rotation speed $E_r/|E_g|$. The outcome can be classified into two types: the case in which fragmentation is observed during the collapse (yellow background) and that in which the collapse proceeds monolithically without fragmentation (blue background). As seen in Section 3.2, rotation facilitates the fragmentation. Thus, rapidly rotating clouds form a ring-like structure and then fragment. Also the separation among the fragments tends to be larger for clouds with faster rotation as seen for the cases without magnetic field (leftmost column of Fig. 12). In our case, fragmentation takes place through the ring formation due to our choice of small initial density fluctuations of about 1 per cent. If large enough density fluctuations are assumed, the fragmentation instead would occur via bar-like structure (Machida et al. 2008b). It is, however, known that the amplitude of initial seed fluctuation does not significantly affect the fragmentation condition while it determines the mode of fragmentation. A large magnetic field suppresses fragmentation through the angular momentum transport (Section 3.2) and causes monolithic collapse. As seen in Fig. 12, fragmentation occurs in cases where the rotation energy E_r is larger than the magnetic field energy E_m and vice versa. If those two values are close $E_r \sim E_m$, fragments, if any, immediately merge due to the small separation. Here, we denote the models that show such evolution as merger models, examples of which are the cases with $(E_r/|E_g|, E_m/|E_g|) = (10^{-4}, 2 \times 10^{-3})$ and $(10^{-6}, 0)$.

3.3.2 Outflow conditions

Next we see the condition for the outflow launching. The density and temperature structure in the x–z plane is shown in Fig. 13 at the same epoch as in Fig. 12. The thick white lines indicate the outflow regions where the velocity in the z direction is outward. We can see that outflows are launched in all the monolithic collapse models and one merger model $(E_r/|E_g|, E_m/|E_g|) = (10^{-4}, 2 \times 10^{-3})$, where a single protostar is formed (Fig. 12). Two types of outflow are known: the magneto-centrifugal wind, which is driven by the centrifugal force along magnetic field lines, and the magnetic-pressure wind, which is driven by the magnetic-pressure gradient force (Tomisaka 2002; Banerjee & Pudritz 2006; Machida et al. 2008a). The magneto-centrifugal wind is launched from a cloud with a strong initial field when the magnetic energy exceeds the thermal energy in the central region (Machida et al. 2008a). In our case, this wind mode becomes dominant for the models with $E_m/|E_g| \geq 2 \times 10^{-3}$, where the field is sufficiently amplified during the collapse. In Fig. 12, we can identify V-shaped density structures in these models, which are characteristic for the magneto-centrifugal winds (Tomisaka 2002). On the other hand, the magnetic-pressure-driven wind can be launched even from clouds with initially weak fields by winding up the field lines many times by the rotation. Once enough magnetic pressure gradient force is built up to overcome the gravity, winds can be driven. An example can be observed in the case with $(E_r/|E_g|, E_m/|E_g|) = (10^{-6}, 2 \times 10^{-5})$, whose structure is similar to the so-called magnetic bubble (Tomisaka 2002). In this case, a large part of the outflow region is occupied by a toroidal rather than a poloidal field, which is a typical magnetic field configuration for the magnetic-pressure-driven wind (Machida et al. 2008a; Tomida et al. 2013).

In any magnetic outflow mechanism, the rotational motion is crucial for the outflow launching. When the gas at a small radius around the protostar has sufficiently large angular momentum, the field lines can be immediately wound up and the outflow is launched. On the other hand, a disc takes time to wind up the field lines. For this reason, we cannot see the outflow from the disc in the fragmentation model just after the protostar formation. Also in these

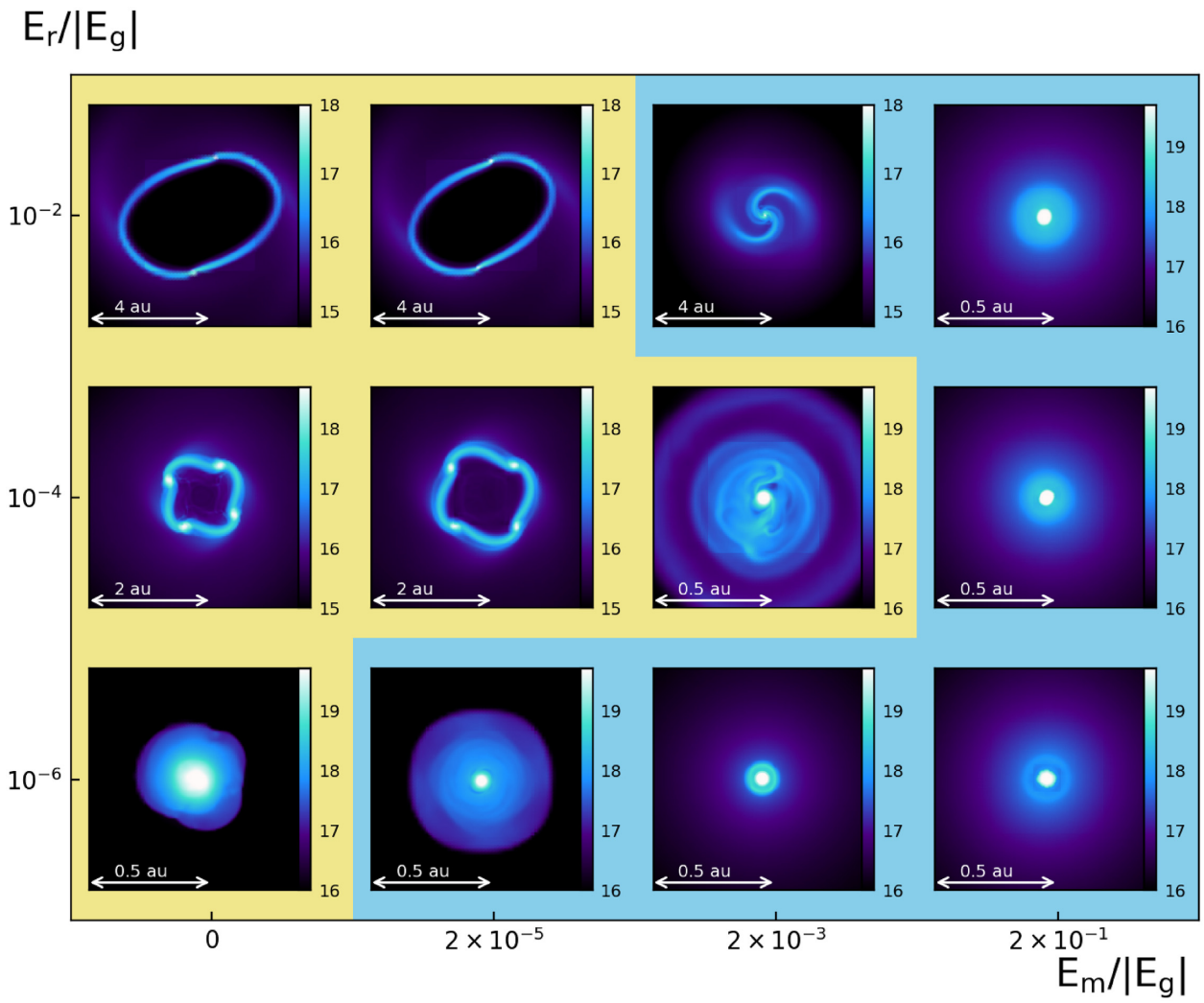

Figure 12. The equatorial density structures just after the protostar formation plotted against $E_m/|E_g|$ and $E_r/|E_g|$. Fragmentation occurs in the models on the yellow background, whereas the cloud monolithically collapses until the protostar formation in the models on the blue background. The colour scale represents $\log n_H$ [cm^{-3}].

models, outflows are not launched from the protostars until the end of our simulation since most of the angular momentum is in the orbital motion.

In summary, a magneto-centrifugal wind is launched just after the protostar formation if $E_m/|E_g| \geq 2 \times 10^{-3}$. Even in the case with a weaker field, if a single protostar is formed due to the effect of magnetic braking, rotation of the protostar immediately winds up the field lines, and as a result magnetic-pressure-driven winds can be launched. Note, however, that even in cases where we did not observe outflows, the magnetic-pressure-driven winds may be driven in a later phase if we follow longer term evolution.

3.4 Comparison with barotropic simulation

Finally, we compare the results of our simulations in which the gas dynamics and thermal evolution are consistently solved with those assuming the barotropic equation of state derived from the one-zone calculation, which is frequently adopted in previous works (e.g. Machida et al. 2008c). The temperature evolution obtained from the one-zone model is that of the cloud centre calculated under the assumption of nearly free-fall collapse. In this section, we first examine how much the temperature in the self-consistent simulation deviates from that derived from the one-zone calculation. We then compare the fragmentation and outflow conditions in the two types of simulations and discuss the validity of the barotropic approximation. In Figs 14 and 15, we show the face-on and edge-on snapshots at the protostar formation for the barotropic simulations, as in Figs 12 and 13, for comparison.

First of all, we consider the difference in the temperature structure between these two simulations. Although the temperature evolution at the centre does not largely deviate from the barotropic case (Fig. 3), the temperature in outer regions can be very different due to the effects such as shock heating by the accretion and outflows (Fig. 13). For example, in the cases of $(E_r/|E_g|, E_m/|E_g|) = (10^{-4}, 0)$ and $(10^{-4}, 2 \times 10^{-5})$, the disc surface is heated by the accretion shock. In the cases of $(E_r/|E_g|, E_m/|E_g|) = (10^{-2}, 0), (10^{-2}, 2 \times 10^{-5})$, and $(10^{-2}, 2 \times 10^{-3})$, hot regions of 4×10^3 K spread above the disc since the H_2 is destroyed by a shock at $z = 70$ au. In all the cases with outflows in Fig. 13, the outflow cavities are heated up to 10^4 K by the shocks. In the model $(E_r/|E_g|, E_m/|E_g|) = (10^{-6}, 0)$, in which an optically thick ring is formed, the ring is heated by the shock and deforms to a hot bubble structure. Needless to say, the

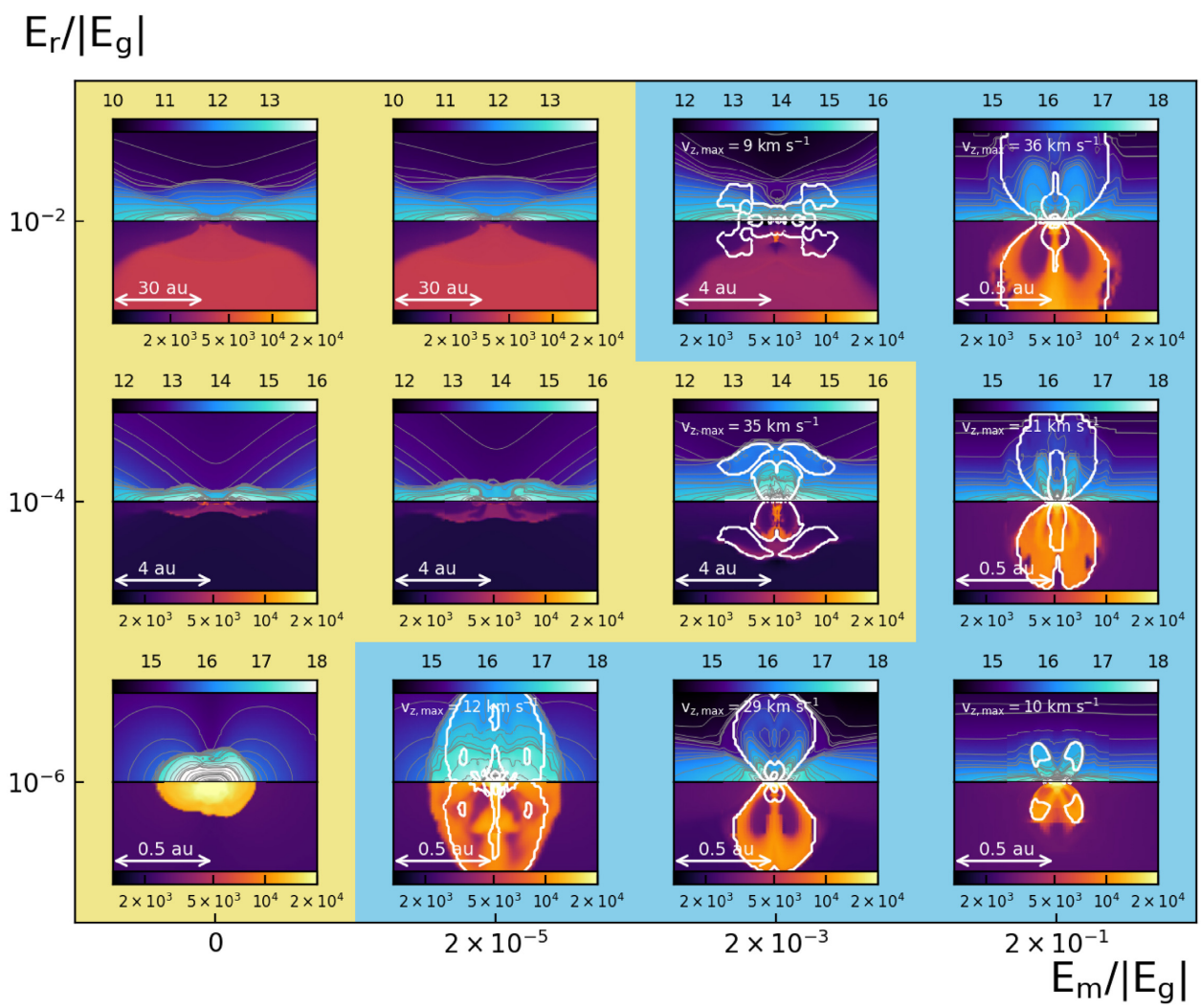

Figure 13. Same as Fig. 12, but for the vertical density and temperature structures. The colour scales represent $\log n_H$ [cm^{-3}] (upper) and T [K] (lower). Thick white contours indicate the outflow regions, with the thin lines in the upper half of each panel representing the density contours. The maximum outflow velocity in the z-direction are shown in each panel.

barotropic simulations cannot reproduce the shock heating as seen in Fig. 13.

Next, we discuss the effect of the temperature difference on the fragmentation. From the comparison of Figs 12 and 14, we can see that cases in which fragmentation occur or not are the same, except for a single case $(E_r/|E_g|, E_m/|E_g|) = (10^{-2}, 2 \times 10^{-3})$. In this model, the temperature of the disc is cooled by the H_2 CIE and adiabatic expansion and the disc becomes gravitationally unstable. As a result, the $m = 2$-mode fluctuation grows rapidly and an arm structure appears. Despite a largely different thermal structure in outer regions, the fragmentation condition remains almost the same among the two sets of simulations since the fragmentation tends to happen in the densest core region where the temperature difference is small. Note also that the final outcomes of the merger models $(E_r/|E_g|, E_m/|E_g|) = (10^{-4}, 2 \times 10^{-3})$ and $(10^{-6}, 0)$ differ: the protostars in the self-consistent simulation have larger radii owing to the shock heating and merge immediately in the realistic simulation (Fig. 12), while they do not in the barotropic simulation (Fig. 14).

Finally, we discuss the effect on outflows. Comparing Figs 13 and 15, we see again that the cases in which the outflows are present are the same among two sets of simulations, even though the surrounding thermal structure is significantly different because of the shock heating. This implies that the thermal structure near the centre controls the outflow driving. The strength of the outflow, however, is different: the flows are weaker in the self-consistent simulations. For the case with $(E_r/|E_g|, E_m/|E_g|) = (10^{-2}, 2 \times 10^{-1})$, the maximum velocity in the z-direction is $v_{z,max} = 36$ km s^{-1} in the self-consistent simulation, while $v_{z,max} = 79$ km s^{-1} in the barotropic simulation. This is because the protostellar radius is larger in the self-consistent simulation due to the shock heating and thus the depth of the gravitational potential well is shallower. This results in the smaller escape (and outflow) velocity.

4 SUMMARY AND DISCUSSION

We have studied the collapse of magnetized primordial clouds starting from the stage of the dense cores with the central density $n_c \simeq 10^3$ cm^{-3} until the protostar formation ($n_c \simeq 10^{20}$ cm^{-3}) with 3D magnetohydrodynamics simulation incorporating self-consistently the thermal processes and non-equilibrium chemical reactions. In this work, we have investigated the effect of magnetic fields on the thermal evolution and fragmentation processes. Besides, we have

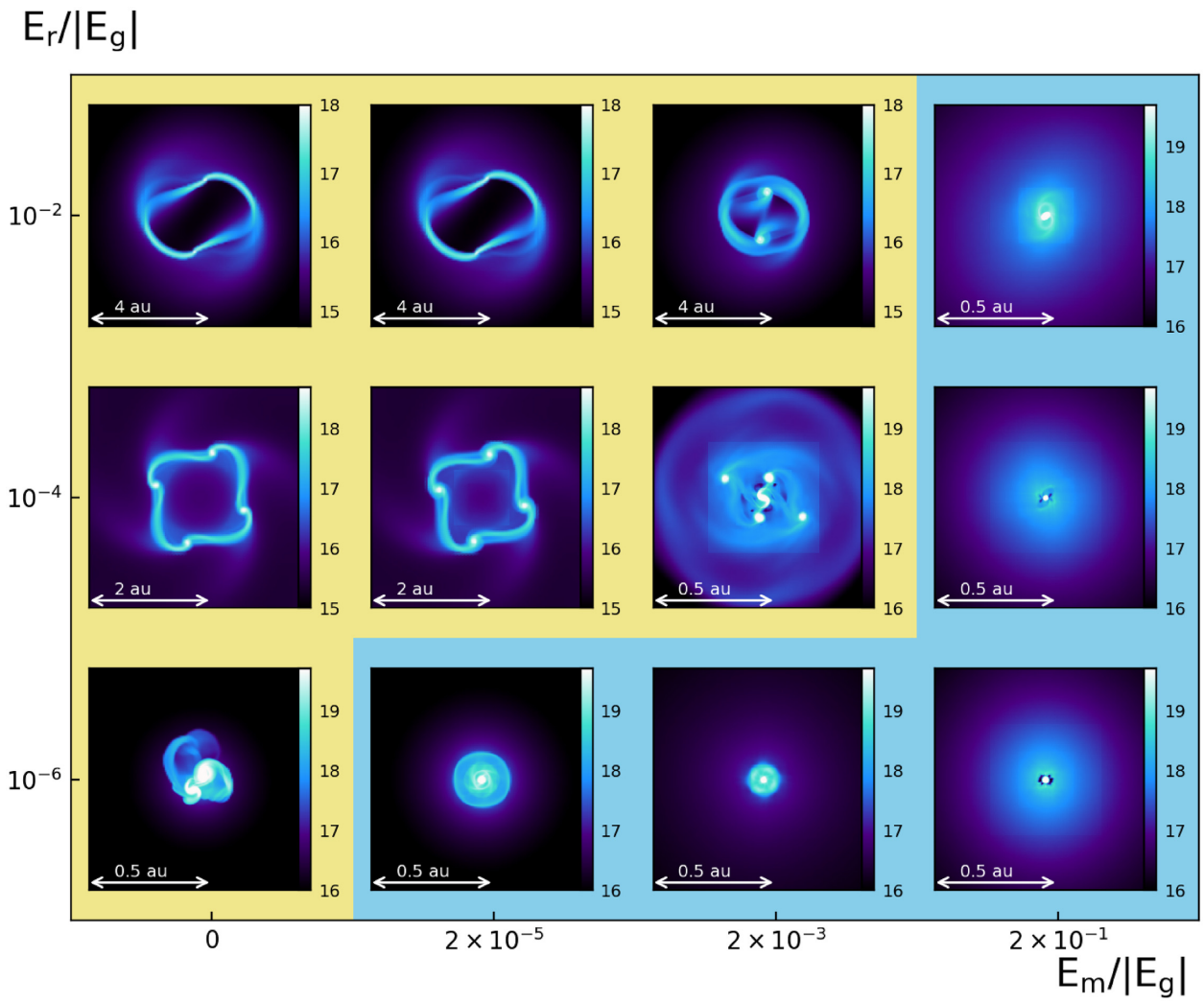

Figure 14. Same as Fig. 12, but for the barotropic simulations.

examined how the fragmentation and outflow launching conditions are altered from simulations using the barotropic approximation. Our findings can be summarized as follows:

(i) Magnetic fields slow down the cloud contraction only in the directions perpendicular to the field lines and not in the parallel directions to them. Also even if the field is amplified and becomes close to the critical value B_{cr} for stopping the gravitational contraction, the cloud deformation due to the magnetic force prevents the fields from reaching the critical value. The collapse always proceeds nearly at the free-fall rate of the central core and the temperature evolution is hardly altered by the magnetic force even in the strong field cases.

(ii) The magnetic braking is the main mechanism that transports angular momentum from collapsing primordial star-forming clouds. If the initial magnetic energy E_m is stronger than rotational energy E_r, the magnetic braking can transport enough angular momentum to prevent a disc formation and its fragmentation. On the other hand, angular momentum transport by the outflows does not affect fragmentation during the pre-stellar collapse since they are launched only in the later phase.

(iii) The fragmentation and outflow launching conditions obtained from our self-consistent simulations are similar to those from the simulations adopting the barotropic equation of state from the one-zone collapse calculation. This is because either magnetic or centrifugal force does not considerably change the central temperature evolution during the collapse, which controls the fragmentation and outflow launching. However, when the initial magnetic field and rotational energies are close, differences in the fragmentation processes are observed due to the differences in thermal evolution caused by the shock heating or cooling processes.

Some effects are not present in the barotropic calculation as we have already mentioned above. For example, the protostellar radius becomes larger due to the shock heating at the stellar surface, which facilitates the merger of protostars. Also, after the protostar formation, temperature in the disc may be different from that in the barotropic simulation. Although the barotropic approximation is good enough during the collapse phase, the gas dynamics and thermal evolution need to be solved consistently for the later phase, in which the radiation from the protostar plays an important role as a feedback.

First-star-forming clouds have rotational energy of about $E_r/|E_g| = 10^{-2}$–10^{-1} according to previous cosmological simulations (e.g. Hirano et al. 2014), roughly corresponding to the cases of $E_r/|E_g| = 10^{-2}$ in our calculation. With this level of rotation, our results indicate that the magnetic field effect becomes important for

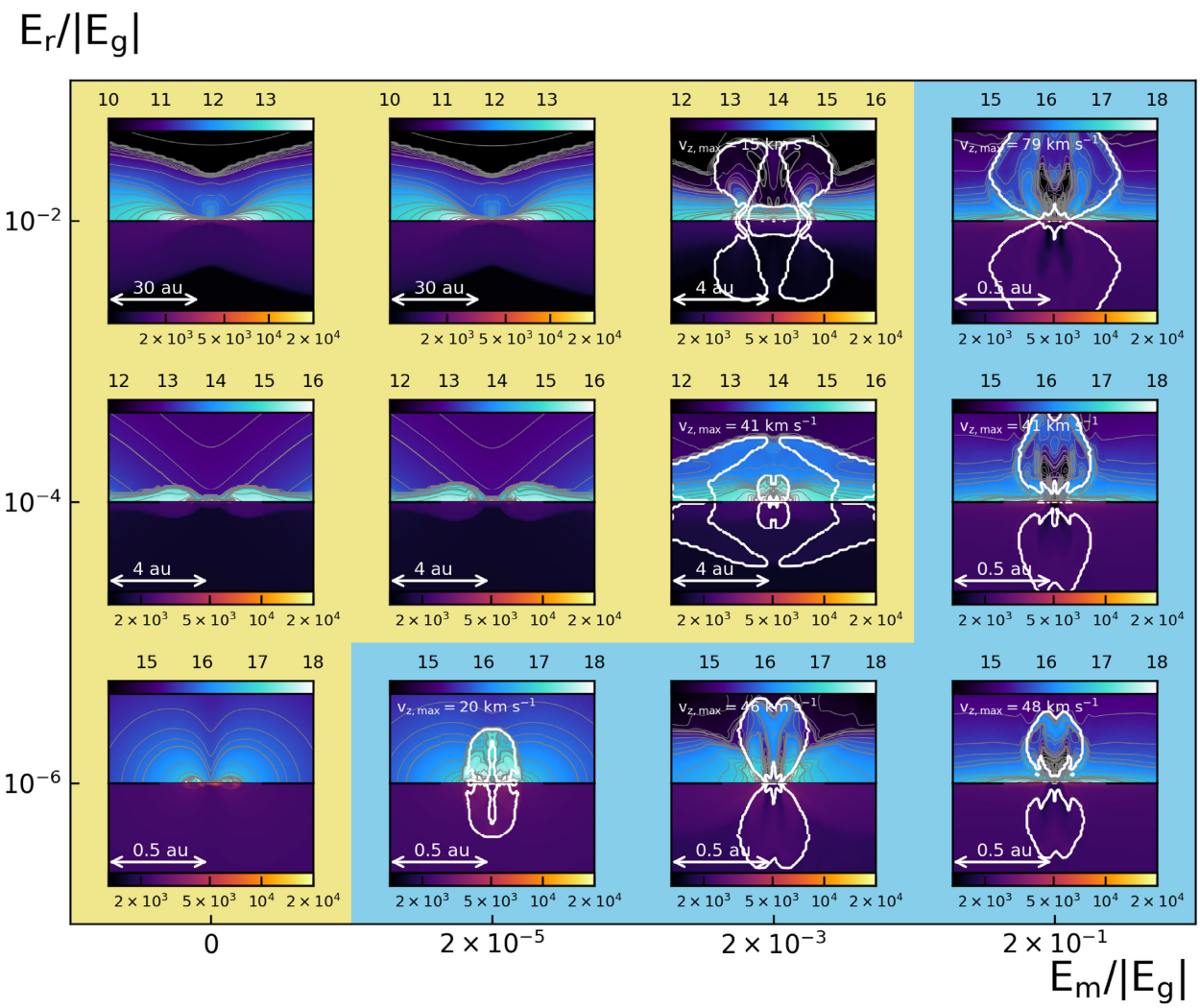

Figure 15. Same as Fig. 13, but for the barotropic simulations.

$B > 10^{-6}(n_c/10^3\ \mathrm{cm}^{-3})^{2/3}$ G during the collapse phase, considering the amplification law in the weak field case $B \propto n_c^{2/3}$. Theoretically, the cosmological fluctuations during the epoch of recombination (Ichiki et al. 2006) or curved shocks in a minihalo (Xu et al. 2008) can produce a uniform primordial magnetic field of at most 10^{-18} G (Ichiki et al. 2006). From these results, we can see that such a uniform week field do not affect the cloud evolution during the collapse phase.

If the gas in a minihalo is highly turbulent, however, the primordial field can be amplified to the critical value by a small-scale dynamo during the collapse phase (Schober et al. 2012) and may affect first-star formation. In this case, the produced magnetic field would have a highly tangled configuration. In the context of present-day star formation, numerical simulations demonstrated that such a tangled field tends to reduce magnetic braking efficiency and leads to form a larger disc (e.g. Seifried et al. 2012; Joos et al. 2013; Tsukamoto 2016). In addition, when the fields are completely tangled without any uniform field component, outflows strong enough to affect the stellar mass is hard to be launched (Gerrard, Federrath & Kuruwita 2019). Therefore, we need to investigate effects of field configuration on first-star formation in future works.

In our simulations, we have assumed ideal MHD since the field dissipation in the primordial gas is ineffective due to higher ionization degree than in the present-day case (Maki & Susa 2004, 2007; Nakauchi et al. 2019). However, if the field is amplified to the critical field strength by a turbulence or a rotational motion in the accretion phase, the ambipolar diffusion may become important in the primordial gas (Schleicher et al. 2009; Nakauchi et al. 2019). The non-ideal effects have been well investigated in the present-day star formation (e.g. Machida, Inutsuka & Matsumoto 2006; Tomida, Okuzumi & Machida 2015; Vaytet et al. 2018), and it is known that the dissipation processes affect the disc and binary evolution by reducing the magnetic braking. Therefore, future study for accretion phase of first star formation should also consider this dissipation effect.

The effects of MHD outflows during the accretion phase have already been studied for the present-day star formation with high accretion rate, $\dot{M} \sim 10^{-3}$–$10^{-2}\ M_\odot\ \mathrm{yr}^{-1}$ (e.g. Matsushita et al. 2017; Machida & Hosokawa 2020). They have suggested that a massive outflow appears only when the initial cloud is strongly magnetized, i.e. $E_m/|E_g| \geq 0.1$. On the other hand, with weaker fields, the outflows, even if launched, are weakened by ram pressure of the accretion flow in the course of propagation in the cloud (Machida & Hosokawa 2020). Their results indicate that all outflows seen in our simulations do not necessarily grow enough to affect the star formation efficiency. However, we cannot directly apply their results to the first star formation because the outflow speeds and launching

scales are largely different from the present-day star formation due to the different thermal evolution. In addition, the outflows are also launched from the first core scale in the present-day case.

For the first star formation, the ionization feedback from a protostar also has a significant effect on limiting its growth (e.g. McKee & Tan 2008; Hosokawa et al. 2011). Both the power of the ionization feedback and the MHD outflow depend on the strength of the accretion rate, and there would be mutual interaction between these two effects. Therefore, in the future, we need to perform radiative MHD simulation taking into account both those effects in the accretion phase to reveal the effect of magnetic fields on the nature of the first stars.

ACKNOWLEDGEMENTS

The authors would like to thank Masahiro Machida and Sunmyon Chon for their helpful comments and discussion. We also thank Daisuke Nakauchi and Ryoki Matsukoba for providing the modules for chemical network and cooling processes. KES acknowledges financial support from the Graduate Program on Physics for Universe of Tohoku University. KS appreciates the support by the Fellowship of the Japan Society for the Promotion of Science for Research Abroad. The numerical simulations were performed on the Cray XC50 at CfCA of the National Astronomical Observatory of Japan, the computer cluster Draco at Frontier Research Institute for Interdisciplinary Sciences of Tohoku University, and the Cray XC40 at Yukawa Institute for Theoretical Physics in Kyoto University. This work was supported in part by the Grant-in-Aid from the Ministry of Education, Culture, Sports, Science and Technology (MEXT) of Japan (KO: 17H02869 and17H01102; TM: 18H05436 and 18H05437; KT: 16H05998 and 18H05440).

DATA AVAILABILITY

The data underlying this article will be shared on reasonable request to the corresponding author.

REFERENCES

Abel T., Bryan G. L., Norman M. L., 2002, Science, 295, 93
Attia O., Teyssier R., Katz H., Kimm T., Martin-Alvarez S., Ocvirk P., Rosdahl J., 2021, MNRAS, 504, 2346
Banerjee R., Jedamzik K., 2004, Phys. Rev. D, 70, 123003
Banerjee R., Pudritz R. E., 2006, ApJ, 641, 949
Baym G., Bödeker D., McLerran L., 1996, Phys. Rev. D, 53, 662
Biermann L., 1950, Z. Nat.forsch. A, 5, 65
Blandford R. D., Payne D. G., 1982, MNRAS, 199, 883
Bonnor W. B., 1956, MNRAS, 116, 351
Brandenburg A., Subramanian K., 2005, Phys. Rep., 417, 1
Bromm V., Coppi P. S., Larson R. B., 2002, ApJ, 564, 23
Chon S., Hosokawa T., 2019, MNRAS, 488, 2658
Ciardi B., Ferrara A., 2005, Space Sci. Rev., 116, 625
Clark P. C., Glover S. C. O., Smith R. J., Greif T. H., Klessen R. S., Bromm V., 2011, Science, 331, 1040
Couchman H. M. P., Rees M. J., 1986, MNRAS, 221, 53
Dedner A., Kemm F., Kröner D., Munz C.-D., Schnitzer T., Wesenberg M., 2002, J. Comput. Phys., 175, 645
Doi K., Susa H., 2011, ApJ, 741, 93
Durrer R., Neronov A., 2013, A&A Rev., 21, 62
Ebert R., 1955, ZAp, 37, 217
Federrath C., Sur S., Schleicher D. R. G., Banerjee R., Klessen R. S., 2011, ApJ, 731, 62
Fukushima H., Omukai K., Hosokawa T., 2018, MNRAS, 473, 4754
Galli D., Shu F. H., 1993, ApJ, 417, 220
Gerrard I. A., Federrath C., Kuruwita R., 2019, MNRAS, 485, 5532
Glover S. C. O., 2015, MNRAS, 453, 2901
Gnedin N. Y., Ferrara A., Zweibel E. G., 2000, ApJ, 539, 505
Greif T. H., 2015, Comput. Astrophys. Cosmol., 2, 3
Hanayama H., Takahashi K., Kotake K., Oguri M., Ichiki K., Ohno H., 2005, ApJ, 633, 941
Hirano S., Hosokawa T., Yoshida N., Umeda H., Omukai K., Chiaki G., Yorke H. W., 2014, ApJ, 781, 60
Hosokawa T., Omukai K., Yoshida N., Yorke H. W., 2011, Science, 334, 1250
Hosokawa T., Hirano S., Kuiper R., Yorke H. W., Omukai K., Yoshida N., 2016, ApJ, 824, 119
Ichiki K., Takahashi K., Ohno H., Hanayama H., Sugiyama N., 2006, Science, 311, 827
Joos M., Hennebelle P., Ciardi A., Fromang S., 2013, A&A, 554, A17
Kimura K., Hosokawa T., Sugimura K., 2021, ApJ, 911, 52
Kinugawa T., Inayoshi K., Hotokezaka K., Nakauchi D., Nakamura T., 2014, MNRAS, 442, 2963
Kinugawa T., Miyamoto A., Kanda N., Nakamura T., 2016, MNRAS, 456, 1093
Kulsrud R. M., Cen R., Ostriker J. P., Ryu D., 1997, ApJ, 480, 481
Langer M., Puget J.-L., Aghanim N., 2003, Phys. Rev. D, 67, 043505
Larson R. B., 1969, MNRAS, 145, 271
Lipovka A., Núñez-López R., Avila-Reese V., 2005, MNRAS, 361, 850
Machida M. N., Hosokawa T., 2020, MNRAS, 499, 4490
Machida M. N., Inutsuka S.-i., Matsumoto T., 2006, ApJ, 647, L151
Machida M. N., Inutsuka S.-i., Matsumoto T., 2008a, ApJ, 676, 1088
Machida M. N., Omukai K., Matsumoto T., Inutsuka S.-I., 2008b, ApJ, 677, 813
Machida M. N., Matsumoto T., Inutsuka S.-I., 2008c, ApJ, 685, 690
McKee C. F., Tan J. C., 2008, ApJ, 681, 771
Maki H., Susa H., 2004, ApJ, 609, 467
Maki H., Susa H., 2007, PASJ, 59, 787
Marchand P., Tomida K., Tanaka K. E. I., Commerçon B., Chabrier G., 2020, ApJ, 900, 180
Matsukoba R., Takahashi S. Z., Sugimura K., Omukai K., 2019, MNRAS, 484, 2605
Matsumoto T., 2007, PASJ, 59, 905
Matsumoto T., Tomisaka K., 2004, ApJ, 616, 266
Matsumoto T., Dobashi K., Shimoikura T., 2015, ApJ, 801, 77
Matsushita Y., Machida M. N., Sakurai Y., Hosokawa T., 2017, MNRAS, 470, 1026
Miyoshi T., Kusano K., 2005, AGU Fall Meeting Abstracts. pp. SM51B–1295
Mouschovias T. C., Paleologou E. V., 1979, ApJ, 230, 204
Mouschovias T. C., Spitzer L. J., 1976, ApJ, 210, 326
Nakauchi D., Omukai K., Susa H., 2019, MNRAS, 488, 1846
Omukai K., Nishi R., 1998, ApJ, 508, 141
Omukai K., Palla F., 2003, ApJ, 589, 677
Omukai K., Tsuribe T., Schneider R., Ferrara A., 2005, ApJ, 626, 627
Omukai K., Hosokawa T., Yoshida N., 2010, ApJ, 722, 1793
Pakmor R. et al., 2017, MNRAS, 469, 3185
Penston M. V., 1969, MNRAS, 144, 425
Quashnock J. M., Loeb A., Spergel D. N., 1989, ApJ, 344, L49
Schleicher D. R. G., Galli D., Glover S. C. O., Banerjee R., Palla F., Schneider R., Klessen R. S., 2009, ApJ, 703, 1096
Schober J., Schleicher D., Federrath C., Glover S., Klessen R. S., Banerjee R., 2012, ApJ, 754, 99
Seifried D., Banerjee R., Pudritz R. E., Klessen R. S., 2012, MNRAS, 423, L40
Sharda P., Federrath C., Krumholz M. R., 2020, MNRAS, 497, 336
Sharda P., Federrath C., Krumholz M. R., Schleicher D. R. G., 2021, MNRAS, 503, 2014
Smith R. J., Glover S. C. O., Clark P. C., Greif T., Klessen R. S., 2011, MNRAS, 414, 3633
Stacy A., Bromm V., Lee A. T., 2016, MNRAS, 462, 1307
Stahler S. W., Palla F., Salpeter E. E., 1986, ApJ, 302, 590
Subramanian K., 2016, Rep. Prog. Phys., 79, 076901
Sugimura K., Matsumoto T., Hosokawa T., Hirano S., Omukai K., 2020, ApJ, 892, L14

Sur S., Schleicher D. R. G., Banerjee R., Federrath C., Klessen R. S., 2010, ApJ, 721, L134
Susa H., 2019, ApJ, 877, 99
Susa H., Hasegawa K., Tominaga N., 2014, ApJ, 792, 32
Tanaka K. E. I., Omukai K., 2014, MNRAS, 439, 1884
Tomida K., Tomisaka K., Matsumoto T., Hori Y., Okuzumi S., Machida M. N., Saigo K., 2013, ApJ, 763, 6
Tomida K., Okuzumi S., Machida M. N., 2015, ApJ, 801, 117
Tomisaka K., 2002, ApJ, 575, 306
Tsukamoto Y., 2016, PASA, 33, e010
Turk M. J., Oishi J. S., Abel T., Bryan G. L., 2012, ApJ, 745, 154
Vaytet N., Commerçon B., Masson J., González M., Chabrier G., 2018, A&A, 615, A5
Xu H., O'Shea B. W., Collins D. C., Norman M. L., Li H., Li S., 2008, ApJ, 688, L57
Yahil A., 1983, ApJ, 265, 1047
Yoshida N., Abel T., Hernquist L., Sugiyama N., 2003, ApJ, 592, 645
Yoshida N., Omukai K., Hernquist L., 2008, Science, 321, 669

This paper has been typeset from a TEX/LATEX file prepared by the author.